



1 **Geochronological and Geochemical Effects of Zircon Chemical Abrasion: Insights from Single-**  
2 **Crystal Stepwise Dissolution Experiments**

3

4 **Alyssa J. McKanna<sup>1,2</sup>, Blair Schoene<sup>1</sup>, and Dawid Szymanowski<sup>1,3</sup>**

5

6 <sup>1</sup>Princeton University, Department of Geosciences, Princeton, New Jersey 08544, USA

7 <sup>2</sup>Los Alamos National Lab, Los Alamos, New Mexico 87545, USA

8 <sup>3</sup>Institute of Geochemistry and Petrology, ETH Zürich, 8092 Zürich, Switzerland

9

10 **Correspondence:** Alyssa J. McKanna (ajmckanna@lanl.gov)

11 **Abstract**

12 Chemical abrasion in hydrofluoric acid (HF) is routinely applied to zircon grains prior to U-Pb  
13 dating by isotope dilution thermal ionization mass spectrometry (ID-TIMS) to remove radiation-  
14 damaged portions of grains affected by Pb loss. Still, many chemically abraded datasets exhibit  
15 evidence of residual Pb loss. Here we test how the temperature and duration of chemical  
16 abrasion affects zircon U-Pb and trace element systematics in a series of 4-hour, single-crystal  
17 stepwise dissolution experiments at 180 °C and 210 °C. Microtextural data for the zircon  
18 samples studied is presented in a complementary paper by McKanna et al. (2023). We find that  
19 stepwise dissolution at 210 °C is more effective at eliminating U, common Pb (Pb<sub>c</sub>), and light  
20 rare earth element (LREE) enriched material affected by open system behavior; reduces the  
21 presence of leaching-induced artefacts that manifest as reverse discordance; and produces  
22 more consistent and concordant results in zircon from the three rocks studied. We estimate  
23 that stepwise dissolution in three 4 h steps is roughly equivalent to a single ~8 h leaching step  
24 due to the insulating properties of the PTFE sleeve in the Parr pressure dissolution vessel,  
25 whereas traditionally labs utilize a single 12-hour leaching step. To better understand the  
26 causes of Pb-loss in zircon, we calculate time-integrated alpha dose estimates for leachates and  
27 residues from measured radionuclide concentrations to determine: 1) the alpha dose of the  
28 material dissolved at the two leaching conditions, and 2) the apparent minimum alpha dose  
29 required for Pb loss to occur:  $\geq 6 \times 10^{17} \alpha/g$ . We conclude that a single 8 h leaching step at 210  
30 °C should yield crystallization ages in the majority of zircon and that this can be used as an  
31 effective approach for routine analysis. However, Ultimately, the effectiveness of any chemical  
32 abrasion protocol will be sample-dependent. By framing Pb loss and zircon solubility in terms of  
33 alpha dose, however, workers can better tailor the chemical abrasion process to specific zircon  
34 samples to improve the accuracy and precision of U-Pb results.

35

36 **1. Introduction**

37 Zircon U-Pb geochronology by isotope dilution thermal ionization mass spectrometry (ID-TIMS)  
38 has played a pivotal role in constraining the timing and tempo of processes on Earth from the  
39 Hadean to the Pleistocene. Zircon is a remarkable chronometer, in part because crystalline  
40 zircon is exceptionally chemically and physically durable. The zircon structure, however, can  
41 accumulate radiation damage over time. Radiation damage is principally caused by alpha recoil



42 events in the  $^{238}\text{U}$ ,  $^{235}\text{U}$ , and  $^{232}\text{Th}$  decay series and the spontaneous fission of  $^{238}\text{U}$  (Ewing et al.,  
43 2003; Meldrum et al., 1998; Weber, 1990). Radiation-damaged zircon can lose Pb and less  
44 commonly U, violating the basic requirement of geochronology that neither parent nor  
45 daughter isotopes are lost through time except through radioactive decay (Geisler et al., 2002).  
46 Fortunately, the dual  $^{238}\text{U}/^{206}\text{Pb}$  and  $^{207}\text{Pb}/^{235}\text{U}$  decay schemes provide a self-check mechanism  
47 by which open system behavior can be identified in zircons older than several hundred Ma  
48 (Mezger and Krogstad, 1997; Corfu, 2013). In the Phanerozoic, however, the dual decay system  
49 becomes less effective at recognizing Pb-loss, since the trajectory of Pb-loss follows Concordia,  
50 and the precision of  $^{207}\text{Pb}/^{235}\text{U}$  dates is also lower than corresponding  $^{238}\text{U}/^{206}\text{Pb}$  dates due to  
51 the shorter radioactive half-life of  $^{235}\text{U}$  and lower isotopic abundance (Corfu, 2013; Schoene,  
52 2014).

53 In a seminal study, Mattinson (2005, 2011) – building off the previous findings of Krogh and  
54 Davis (1975) and Todt and Büsch (1981) – demonstrated that the most radiation-damaged  
55 portions of zircon can be effectively removed by hydrofluoric acid through a series of stepwise  
56 dissolution experiments on multi-grain aliquots. He showed that early leaching steps sampled  
57 high-U material with discordant U-Pb dates, while later leaching steps sampled low-U residues  
58 unaffected by open-system behavior. Mattinson (2005, 2011) further established that partially  
59 annealing zircon samples prior to leaching helps to minimize the unwanted isotopic  
60 fractionation effects that plagued earlier leaching attempts (Davis & Krogh, 2000; Todt &  
61 Büsch, 1981). These experimental findings revolutionized the field of zircon U-Pb  
62 geochronology by allowing scientists to attain meaningful geochronological results from  
63 previously unusable zircon affected by open-system behavior. Air abrasion – the pre-treatment  
64 technique previously used to remove crystal rims (thought to be high in U) and improve U-Pb  
65 concordance (Krogh, 1981) was largely abandoned. Today, a variation of Mattinson’s approach –  
66 termed chemical abrasion – is applied to virtually all zircon grains prior to ID-TIMS U-Pb isotopic  
67 analysis. In this variation, zircon crystals are annealed at 800 °C to 1200 °C for 36 h to 60 h and  
68 then leached in concentrated HF at 180 °C to 210 °C for 10 h to 18 h prior to dissolution and  
69 isotopic analysis (Mundil et al., 2004; Huyskens et al., 2016; Widmann et al., 2019).

70 The decrease in sample size from multi-grain aliquots to portions of single crystals and the  
71 concurrent increase in analytical precision in TIMS over the past half-century (e.g., Schoene,  
72 2014) demands a critical re-evaluation of the chemical abrasion technique and the accuracy of  
73 the U-Pb ages that the Earth science community has come to rely on. Many studies have now  
74 shown that chemically abraded zircon samples often exhibit residual Pb-loss. This challenge is  
75 widely recognized in the ID-TIMS U-Pb community and has prompted new investigations into  
76 the effects of different annealing and leaching conditions on geochronological outcomes  
77 (Huyskens et al., 2016; Widmann et al., 2019), new statistical approaches for evaluating over-  
78 dispersed U-Pb datasets (Keller, 2023), and microstructural studies of chemically abraded zircon  
79 (McKenna et al., 2023).

80 We build on earlier work of Mattinson (2005, 2011) and present a series of new stepwise  
81 dissolution experiments performed at the single-crystal scale. We evaluate the effects of  
82 stepwise chemical abrasion at 180 °C and 210 °C on zircon U-Pb and trace element systematics



83 in three zircon samples – AS3, SAM-47, and KR18-04 – which span a range of crystallization  
84 ages, geological settings, and radiation damage densities. These zircons come from the same  
85 sample aliquots as studied by McKanna et al. (2023) in their recent microstructural  
86 investigation of zircon dissolution which presents a unique opportunity to integrate zircon  
87 microtextures, geochronology, and geochemistry.

## 88 2. Methods

89  
90 Zircon samples were annealed in quartz crucibles at 900 °C for 48 h in air in a box furnace prior  
91 to the start of the experiments. Annealed grains were mounted in epoxy, polished, and imaged  
92 by cathodoluminescence (CL) or backscattered electron (BSE) imaging using a XL30 FEG  
93 scanning electron microscope equipped with a mini-Gatan CL detector and a semiconductor  
94 BSE detector housed at the PRISM Imaging and Analysis Center at Princeton University.  
95 Representative images of AS3, SAM-47, and KR18-04 crystals can be found in McKanna et al.  
96 (2023) Fig. 3 and Fig. 4.

97  
98 The stepwise partial dissolution protocol outlined here is very similar to that of Keller et al.,  
99 (2019, their Fig. 1). Crystals were plucked from their epoxy mounts, rinsed in 30% HNO<sub>3</sub>, and  
100 individually transferred to 200 μL PFA microcapsules for partial dissolution in ~100 μL of  
101 concentrated HF. Microcapsules were loaded into a PTFE-lined Parr pressure dissolution vessel  
102 with 5 mL moat HF and placed in a box oven set to 180 °C or 210 °C for a period of 4 h. At the 4  
103 h mark, the pressure vessel was removed from the oven and placed in front of a fan to cool to  
104 room temperature.

105  
106 The microcapsules were then removed from the pressure vessel and the leachate (the dissolved  
107 zircon-HF mixture) from each microcapsule was transferred to a clean 7 mL PFA beaker using a  
108 pipette. A fresh, acid-cleaned pipette tip was used for each sample transfer. Approximately 100  
109 μL of 6N HCl was added to the residue (the remaining undissolved zircon) in the microcapsule,  
110 and the microcapsule was capped and placed on the hotplate for 1 h. The 6N HCl was then  
111 pipetted off the residue and added to the 7 mL PFA beaker with the sample leachate. The  
112 residue was then sequentially rinsed in the microcapsule using a pipette with 3N HCl, 6N HCl,  
113 30 % HNO<sub>3</sub>, and concentrated HF. These rinses were discarded. About 100 μL of fresh  
114 concentrated HF was then added to each residue for the second round of step leaching. In total,  
115 samples were partially dissolved in a series of three 4-h leaching steps generating a L1, L2, and  
116 L3 leachate for each zircon crystal.

117  
118 After the L3 leachate was collected, the residue was again rinsed with acid and ~100 μL of fresh  
119 HF was added to the microcap. Each residue was spiked with the EARTHTIME <sup>205</sup>Pb-<sup>233</sup>U-<sup>235</sup>U  
120 tracer (Condon et al., 2015; McLean et al., 2015) and dissolved in a Parr pressure dissolution  
121 vessel in a box oven at 210 °C for 48 to 60 h. Each leachate was spiked with the same tracer,  
122 capped, and placed on the hot plate for the same duration. Both leachates and residues were  
123 then dried down on the hot plate. Residues were redissolved in ~100 μL of 6N HCl in the Parr  
124 pressure vessel in the box oven at 180 °C overnight, and leachates were redissolved in ~100 μL  
125 of 6N HCl on the hot plate overnight. Afterward, all residues and leachates were dried down on



126 the hot plate and redissolved in 3N HCl in preparation for ion exchange chromatography. This  
127 procedure was modified slightly for half the KR18-04 zircon samples step-leached at 210 °C to  
128 evaluate whether a protocol change could mitigate unwanted U-Pb elemental fractionation  
129 effects as suggested by Mattinson (2005) with the goal of eliminating U-loss caused by the  
130 incomplete dissolution of fluoride salts. For these samples, after each HF leachate was  
131 collected, zircon residues were dried down completely on the hot plate before the addition of  
132 ~100 µL of 6N HCl. Microcaps were then transferred back to the Parr pressure vessel and  
133 redissolved at 180 °C overnight in the box oven. The 6N HCl liquid was then pipetted off the  
134 residue and again added to the sample's HF leachate in the PFA 7 mL beaker. This procedure  
135 was repeated for the L2 and L3 leachates. All other steps remained the same.

136  
137 PTFE columns were prepared with 50 µL of Eichrom AG1-X8 anion exchange resin, cleaned, and  
138 equilibrated. U-Pb ion exchange chemistry followed the protocol established by Krogh (1973)  
139 and modified by Schoene et al., (2010) for the collection of trace elements. Combined U and Pb  
140 fractions were dried down with trace 0.05 M H<sub>3</sub>PO<sub>4</sub> and loaded onto a zone-refined Re filament  
141 with a Si-gel emitter (Gerstenberger & Haase, 1997) for isotopic analysis on one of the two  
142 IsotopX Phoenix TIMS at Princeton University. Pb isotopes were measured on either the  
143 Daly/photomultiplier detector or ATONA Faraday system (Szymanowski and Schoene, 2020),  
144 and U isotopes were measured as oxides on Faraday cups with 10<sup>12</sup> Ω resistors or on the  
145 ATONA Faraday system. Mass fractionation in Pb isotopic analyses was corrected for with  
146 factors specific to each detector system, derived from a compilation of in-run values measured  
147 in double-spiked samples; for U the correction used the known <sup>233</sup>U/<sup>235</sup>U of the tracer. Tripoli  
148 and ET-Redux software (Bowring et al., 2011; McLean et al., 2011) were used for processing  
149 isotopic data and error propagation, assuming a sample <sup>238</sup>U/<sup>235</sup>U ratio of 137.818 ± 0.045 (2σ)  
150 (Heiss et al., 2012). All reported <sup>206</sup>Pb/<sup>238</sup>U and <sup>207</sup>Pb/<sup>206</sup>Pb dates are calculated using the decay  
151 constants of Jaffey et al., (1971) and Th-corrected assuming a magma Th/U ratio of 3.5.  
152 Reported uncertainties reflect 2σ analytical uncertainties. Common Pb corrections assume a  
153 composition equivalent to the blank.

154  
155 Major and trace element analyses were made using a Thermo Scientific iCap-Q inductively  
156 coupled plasma mass spectrometer (ICPMS) at Princeton University following the procedure  
157 developed by Schoene et al., (2010), with analytical parameters described in O'Connor et al.,  
158 (2022) U concentrations were calculated from Th concentrations measured by ICPMS and the  
159 Th/U ratio estimated from radiogenic <sup>208</sup>Pb and the <sup>206</sup>Pb/<sup>238</sup>U age assuming concordance  
160 between the U-Pb and Th-Pb systems. The percent zircon dissolved is calculated using Zr  
161 abundances: (Zr<sub>step</sub>/Zr<sub>total</sub>) × 100. LREE-indices (LREE-I) quantify LREE-enrichment in zircon  
162 which can reflect chemical alteration or sample contamination. The lower the LREE-I, the higher  
163 the LREE-enrichment. LREE-I is calculated as [Dy]/[Nd] + [Dy]/[Sm] following Bell et al., (2016).

164

### 165 **3. Background and results**

166

#### 167 **3.1 AS3**

168

##### 169 **3.1.1 Geologic setting and sample description**



170

171 AS3 zircons are from an anorthosite from the Duluth Complex of northern Minnesota, USA  
172 which formed during the Mesoproterozoic North American Midcontinent Rift (92°09'32.4",  
173 46°45'43.4") (Paces & Miller, 1993; Miller et al., 2002; Schmitz et al., 2003; Swanson-Hysell et  
174 al., 2019, 2020). The Duluth Complex is a massive layered mafic intrusion. The anorthositic and  
175 layered series of the complex were emplaced at ~1096 Ma over a duration <1 m.y. (Swanson-  
176 Hysell et al., 2020). The voluminous magmatism that formed the Duluth Complex is attributed  
177 to decompression melting due to lithospheric extension occurring atop an upwelling magmatic  
178 plume (Swanson-Hysell et al., 2020). Rifting in the region ceased at ~1084 Ma (Swanson-Hysell  
179 et al., 2019). Thermochronology data from Minnesota River Valley in southern Minnesota  
180 suggest that rocks in the region have sat at near-surface temperature conditions since the  
181 Neoproterozoic (Guenther et al., 2013; McDannell et al., 2022).

182

183 The AS3 sample studied is the same as that of Takehara et al., (2018). The rock sample is  
184 composed of plagioclase, amphibole, clinopyroxene, and ilmenite with minor K-feldspar,  
185 apatite, zircon, and baddeleyite. Partially chloritized amphiboles, altered plagioclase, and  
186 zeolite veins indicate that this sample of AS3 has interacted with low-temperature  
187 hydrothermal fluids as previously described (Takehara et al., 2018). Zircon grains are large and  
188 occur as orange-to-orangish brown tabular prisms or anhedral shards. Grains are fractured and  
189 often have large melt inclusions oriented elongate to the *c*-axis. Crystals exhibit concentric and  
190 convolute zonation patterns, and many grains are hydrothermally altered (McKanna et al.,  
191 2023; Takehara et al., 2018). Included and altered grains were included in the experiments to  
192 evaluate how well geochemical data traces the dissolution of inclusions and altered material.  
193 Raman data indicate that grains have accumulated high radiation damage densities with  
194 equivalent alpha doses of  $2 \times 10^{17}$  to  $>1 \times 10^{19}$   $\alpha/g$  with significant intracrystalline variations in  
195 radiation damage (McKanna et al., 2023).

196

### 197 **3.1.2 Previous geochronology**

198

199 Paces and Miller (1993) presented the first U-Pb geochronological data for AS3 zircon. These  
200 authors found that six multi-grain aliquots of air-abraded zircon crystals produced concordant  
201 ID-TIMS U-Pb dates and assigned the sample a weighted-mean  $^{207}\text{Pb}/^{206}\text{Pb}$  age of  $1099.1 \pm 0.5$   
202 Ma ( $2\sigma$ ). Schmitz et al., (2003) later conducted additional ID-TIMS U-Pb isotopic analysis on  
203 individual air-abraded AS3 zircon. The authors found that several crystals produced discordant  
204 dates affected by recent Pb loss. Twelve concordant analyses yielded a concordia age of  $1099.1$   
205  $\pm 0.2$  Ma ( $2\sigma$ ). Eight grains from the same sample were later analyzed by chemical abrasion ID-  
206 TIMS by Schoene et al., (2006) producing concordant dates with weighted mean  $^{206}\text{Pb}/^{238}\text{U}$  and  
207  $^{207}\text{Pb}/^{206}\text{Pb}$  ages of  $1095.9 \pm 0.2$  Ma and  $1098.6 \pm 0.3$  ( $2\sigma$ ), respectively. These grains were  
208 annealed at 900 °C for 60 h and chemically abraded in an HF-HNO<sub>3</sub> mixture at 180 °C for 12 to  
209 14 h. Age differences between these and previous results were attributed by the authors to  
210 differences in tracer calibration, which had been redone as part of (Schoene et al., 2006).  
211 Takehara et al., (2018) later demonstrated that zircons from a different sample of AS3 collected  
212 from the same sample locality are strongly affected by hydrothermal alteration; sensitive high-  
213 resolution ion microprobe (SHRIMP) analyses showed that hydrothermally altered zones

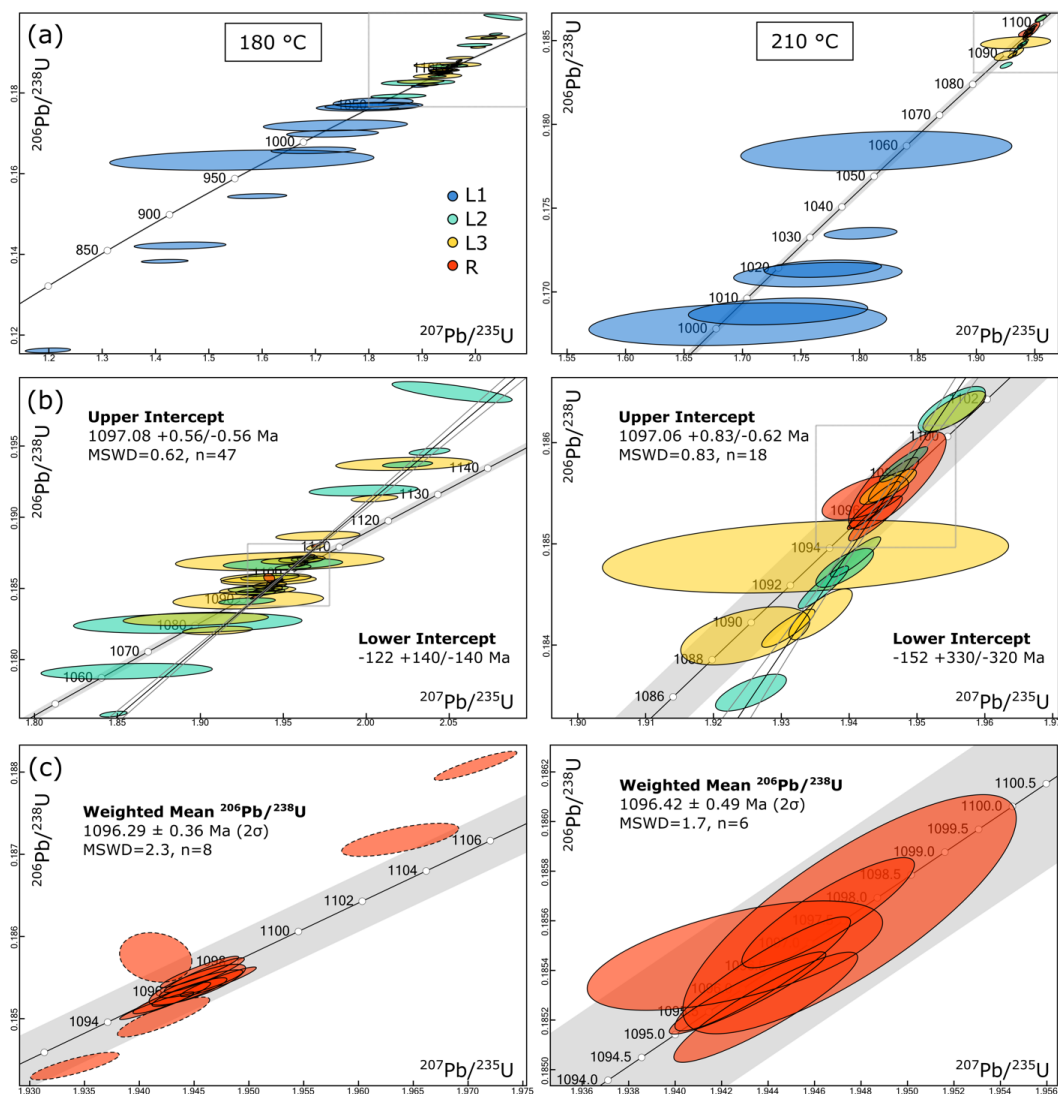


Figure 1. U-Pb concordia diagrams for the 180 °C (left) and 210 °C (right) AS3 experiments. **(a)** All data are depicted except for L1 leachates with  $\text{Pb}^*/\text{Pb}_c$  values < 1. **(b)** Close up of L2, L3, and R data. **(c)** Close up of zircon residue data. Ellipses with dashed borders were excluded from the weighted-mean  $^{206}\text{Pb}/^{238}\text{U}$  age for the 180 °C experiment. All ellipses reflect  $2\sigma$  analytical uncertainties.

214 yielded normally discordant U-Pb analyses, were enriched in incompatible trace elements  
 215 including LREEs, Ca, Mn, Fe, Al, Li, and K, and depleted in Zr and Si.  
 216  
 217  
 218  
 219

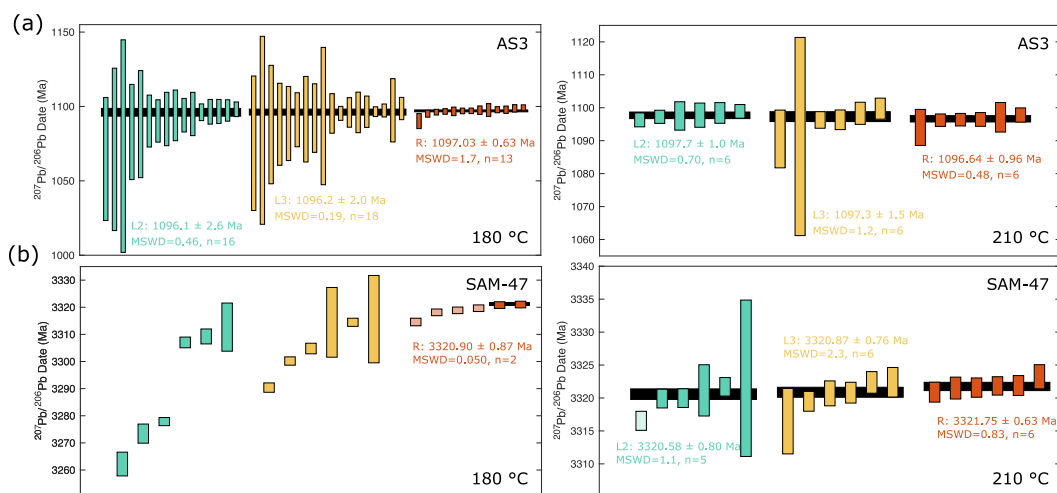


Figure 2. Ranked order  $^{207}\text{Pb}/^{206}\text{Pb}$  dates for the (a) AS3 and (b) SAM-47 experiments. Black bars represent weighted means. Bar heights and quoted uncertainties reflect propagated  $2\sigma$  analytical uncertainties.

### 220 3.1.3 U-Pb and trace element results

221

222 ID-TIMS U-Pb results for AS3 samples are presented in Fig. 1, Fig. 2, and Table S1. L1 leachates  
 223 are younger than zircon residues indicating the dissolution of material strongly affected by Pb  
 224 loss. L1 leachates have large age uncertainties due to high amounts of  $\text{Pb}_c$ . Consequently, many  
 225 large error ellipses overlap the Concordia curve. L1 leachates with higher radiogenic to common  
 226 Pb ( $\text{Pb}^*/\text{Pb}_c$ ) ratios and better age precision are normally discordant. L2 and L3 leachates are  
 227 older than L1 leachates and form a discordia line through analyses that are either normally  
 228 discordant, concordant, or reversely discordant. The upper intercept ages for the discordia lines  
 229 agree within uncertainty with the weighted mean  $^{206}\text{Pb}/^{238}\text{U}$  age for residues treated at 210 °C.  
 230 The lower intercept ages of the discordia lines are zero-age. Ages for L2 and L3 leachates  
 231 treated at 180 °C are more widely dispersed than ages for L2 and L3 leachates treated at 210 °C.  
 232 The 180 °C leachates also have larger uncertainties due to higher  $\text{Pb}_c$  contents.

233

234 Residues treated at 210 °C form a single, concordant age population with weighted mean  
 235  $^{206}\text{Pb}/^{238}\text{U}$  age of  $1096.42 \pm 0.49$  Ma (MSWD = 1.7; Fig. 1) in agreement with previous  
 236 geochronology (Schoene et al., 2006). U-Pb ages of residues treated at 180 °C are dispersed  
 237 along Concordia; a cluster of residue analyses agree with the 210 °C result yielding a weighted  
 238 mean  $^{206}\text{Pb}/^{238}\text{U}$  age of  $1096.29 \pm 0.36$  Ma (MSWD = 2.3), but a few analyses are either older or  
 239 younger. Two of the 180 °C residues are reversely discordant. Weighted-mean  $^{207}\text{Pb}/^{206}\text{Pb}$  ages  
 240 for all leachates and residues agree within uncertainty (Fig. 2). The weighted-mean  $^{207}\text{Pb}/^{206}\text{Pb}$   
 241 ages obtained for the 180 °C and 210 °C residues are  $1097.03 \pm 0.63$  Ma (MSWD = 1.7) and  
 242  $1096.64 \pm 0.96$  Ma (MSWD = 0.48), respectively. These dates are slightly younger than previous  
 243 geochronology (Schoene et al., 2006).

244

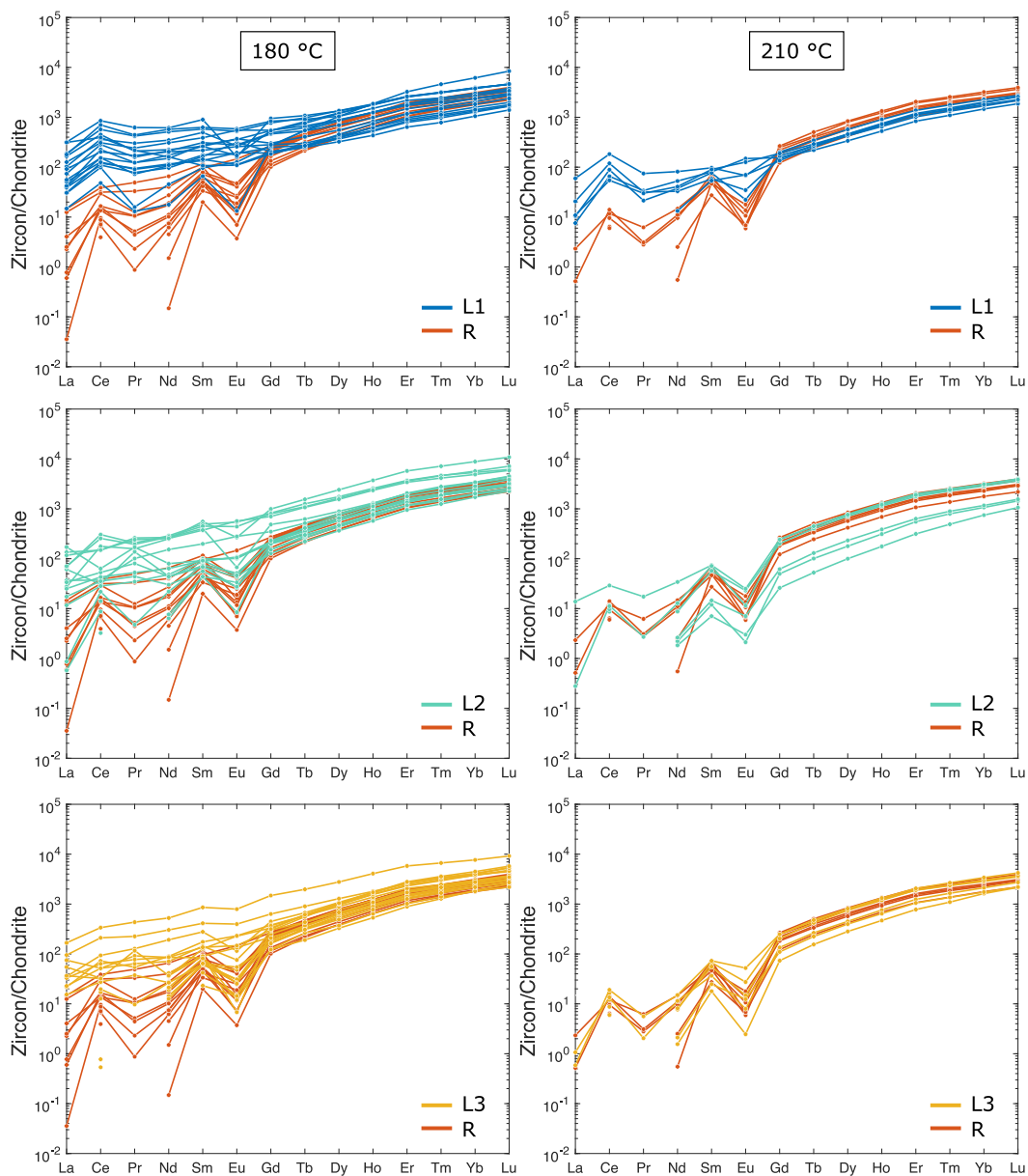


Figure 3. Chondrite-normalized REE spider diagrams for the 180 °C (left) and 210 °C (right) AS3 experiments comparing results for leachates and residues.

245 Leachates from the 180 °C experiment are enriched in LREE,  $Pb_c$ , and U relative to zircon  
246 residues (Fig. 3, Fig. 4, Fig. 5, and Table S2). LREE enrichment is apparent both in chondrite-  
247 normalized REE spider diagrams and in LREE-I values. Sample's LREE-I and radiogenic to

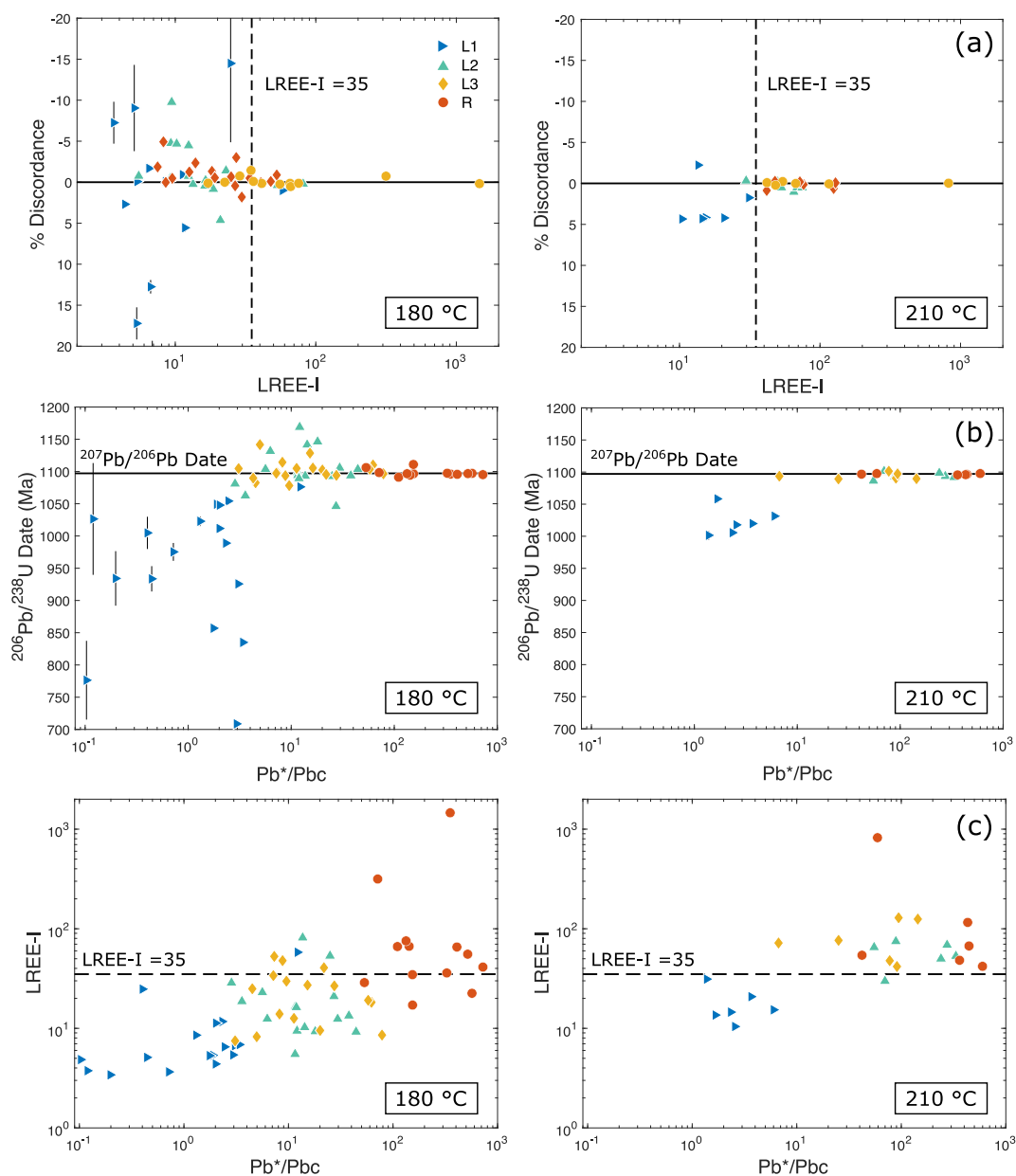


Figure 4. AS3 U-Pb and trace element data for the 180 °C (left) and 210 °C (right) experiments. **(a)** LREE-I versus percent discordance. The horizontal solid line represents perfect concordance. The vertical dashed line depicts a LREE-I threshold value of 35 below which data is notably more discordant. **(b)** <sup>206</sup>Pb/<sup>238</sup>U date plotted as a function of the radiogenic Pb\* to common Pb ratio. Error bars for the percent discordant and <sup>206</sup>Pb/<sup>238</sup>U data reflect propagated 2σ analytical uncertainties. Most error bars are smaller than data markers. **(c)** The radiogenic Pb\* to common Pb ratio versus the LREE-I showing a positive correlation between the two variables.

248 common Pb ratio (Pb\*/Pbc) are clearly correlated. L1 leachates from the 210 °C dataset are

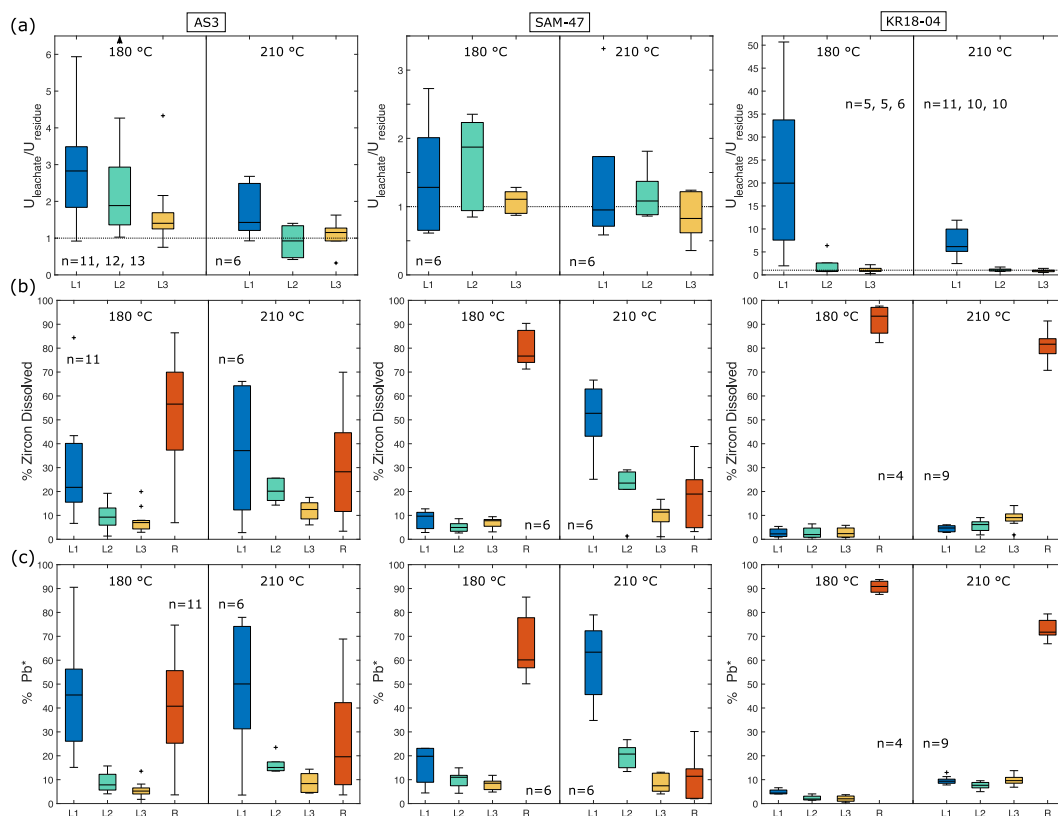


Figure 5. Box plot diagrams depicting geochemistry data for all step-leaching experiments. Each box shows the median value (black bar), the upper and lower quartiles (box), the minimum and maximum values (whiskers), and statistical outliers (plus marks) (a) Uranium concentration of leachates relative to that of their associated residue. (b) Percent zircon dissolved per leaching step based on measured Zr abundances. (c) Percent of radiogenic Pb\* measured per leaching step.

249 similarly enriched in LREE, Pb<sub>c</sub>, and U relative to zircon residues, whereas 210 °C L2 and L3  
 250 leachates have compositions comparable to residues.

251

252 In the majority of samples, most dissolution occurred in the first leaching step with  
 253 progressively smaller volumes dissolved in L2 and L3. The median fraction of the zircon mass  
 254 remaining after L3 for the 180 °C experiment is ~55%, whereas for the 210 °C experiment it is  
 255 ~30%. Percent Pb\* mirrors results for percent zircon dissolved in both experiments.

256

## 257 3.2 SAM-47

258

### 259 3.2.1 Geologic setting and sample description

260 SAM-47 is an Archean (~3.32 - 3.29 Ga) granodiorite from the Corunna Downs Granitic Complex  
 261 of the Emu Pools Supersuite in the eastern Pilbara Craton (-21°24'29.01", 119°46'21.03")



262 (Barley and Pickard, 1999; Smithies et al., 2003; Van Kranendonk et al., 2007). The tectonic  
263 significance of the dome and keel structures of the eastern Pilbara Craton are a matter of  
264 debate, and the region has experienced a multi-phase deformational history (Kloppenborg et  
265 al., 2001; MacLennan, 2019; Moore and Webb, 2013). ID-TIMS U-Pb cooling ages for apatite  
266 from the Corunna Downs Granitic Complex are  $\sim 3.3$  Ga which are similar to Ar-Ar ages reported  
267 by Kloppenburg (2003). The similarity between the U-Pb and Ar-Ar data suggest rapid cooling  
268 through  $\sim 460^\circ\text{C}$  following intrusion of the granitoid (MacLennan, 2019). Zircon (U-Th)/He dates  
269 for the Owen's Gully diorite from the Mount Edgar Granitic Complex north of the Corunna  
270 Downs range from  $677.5 \pm 36.3$  to  $815.5 \pm 44.6$  Ma in age, suggesting that the eastern craton  
271 reached near-surface thermal conditions where radiation damage can accumulate in zircon  
272 sometime in the Neoproterozoic (Magee et al., 2017). Low-temperature thermochronology  
273 data from elsewhere in the Pilbara craton (the northern, central, and western blocks) suggest  
274 that the onset of widespread cooling related to basin-development and unroofing varied  
275 regionally starting sometime between  $\sim 600$  and  $300$  Ma (Morón et al., 2020). Zircon grains  
276 separated from SAM-47 are euhedral, brown, and translucent. Crystals display fine-scale  
277 concentric growth zones (McKanna et al., 2023). Rims are enriched in actinides and radiation  
278 damage relative to cores. Raman data suggest that grains have accumulated intermediate-to-  
279 high radiation damage densities with equivalent alpha doses ranging from  $6 \times 10^{17}$  to  $2 \times 10^{18}$   $\alpha/\text{g}$   
280 (McKanna et al., 2023). There is no previous U-Pb geochronology for zircon from this sample,  
281 however, Pb loss is common in similarly aged zircon from the Pilbara craton (MacLennan, 2019).

### 282 3.2.2 U-Pb and trace element results

283  
284 ID-TIMS U-Pb results for SAM-47 samples are presented in Fig. 2, Fig. 6, and Table S3. L1  
285 leachates from both sample sets are normally discordant resulting in  $^{206}\text{Pb}/^{238}\text{U}$  dates that are  
286  $>800$  Ma. younger than zircon residues, indicating the dissolution of domains strongly affected  
287 by Pb-loss. Although systematically older than L1 leachates, L2 and L3 leachates from the  $180^\circ\text{C}$   
288 experiment are normally discordant. Two residues from the  $180^\circ\text{C}$  dataset are concordant and  
289 have a weighted-mean  $^{206}\text{Pb}/^{238}\text{U}$  age of  $3319.5 \pm 1.4$  Ma (MSWD = 1.7). The remaining four  
290 residues are normally discordant. In contrast to the  $180^\circ\text{C}$  experiment, many of the L2 and L3  
291 leachates from the  $210^\circ\text{C}$  experiment are concordant, and the few normally discordant  
292 analyses closely approach Concordia. All  $210^\circ\text{C}$  residues overlap or closely hug Concordia.  
293 Three of the concordant residues yield a weighted-mean  $^{206}\text{Pb}/^{238}\text{U}$  age of  $3316.1 \pm 1.6$  Ma  
294 (MSWD = 1.0) that is slightly younger than the  $180^\circ\text{C}$  dataset. Upper intercept ages for  $180^\circ\text{C}$   
295 residues,  $210^\circ\text{C}$  residues, as well as  $210^\circ\text{C}$  L2 and L3 leachates all agree within uncertainty and  
296 produce robust MSWDs as shown in Fig. 6. The most precise upper and lower intercept ages are  
297  $3321.23 \pm 0.78/-0.71$  Ma and  $751 \pm 140$  Ma, respectively.

298  
299 Most  $^{207}\text{Pb}/^{206}\text{Pb}$  dates for L2, L3, and R samples from the  $210^\circ\text{C}$  experiment agree within  
300 uncertainty (Fig. 2). The  $210^\circ\text{C}$  residues yield a weighted-mean  $^{207}\text{Pb}/^{206}\text{Pb}$  age of  $3321.75 \pm$   
301  $0.63$  Ma (MSWD = 0.83) which agrees well with our upper intercept ages. In contrast,  
302  $^{207}\text{Pb}/^{206}\text{Pb}$  dates from the  $180^\circ\text{C}$  dataset are notably younger, indicating the dissolution of  
303 domains affected by a Pb loss event that occurred in the distant past. The two concordant  $180$

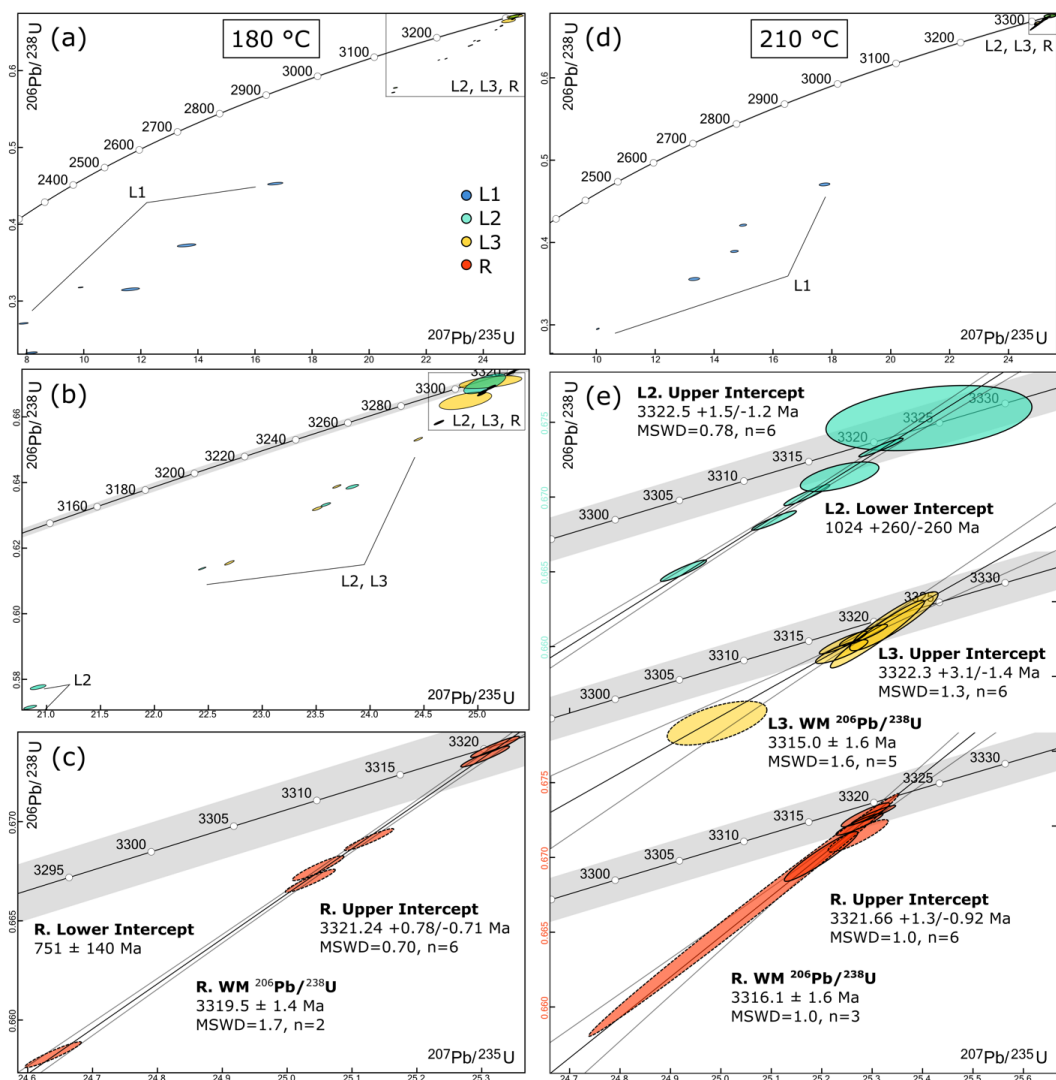


Figure 6. U-Pb concordia diagrams for the SAM-47 180 °C (left) and 210 °C (right) step-leaching experiments. (a) All data for the 180 °C experiment. (b) Close up of the L2, L3, and R 180 °C dataset. (c) Close up of the 180 °C residue data. (d) All data for the 210 °C experiment. (e) Stacked plot showing the L2, L3, and R 210 °C datasets. All ellipses reflect  $2\sigma$  analytical uncertainties. Dashed ellipses are excluded from weighted mean calculations.

304 °C residue analyses yield a weighted-mean  $^{207}\text{Pb}/^{206}\text{Pb}$  age of  $3320.90 \pm 0.87$  (MSWD = 0.050) in  
 305 agreement with the 210 °C results.

306

307 L1, L2, and some L3 leachates from the 180 °C experiment are enriched in LREE and  $\text{Pb}_c$  relative  
 308 to zircon residues (Fig. 7, Fig. 8, and Table S4). Some – but not all – leachates from the 180 °C  
 309 dataset are also marginally enriched in U relative to residues (Fig. 5). The composition of a  
 310 subset of 180 °C L3 leachates closely approximates that of residues. LREE and  $\text{Pb}_c$  enrichment is

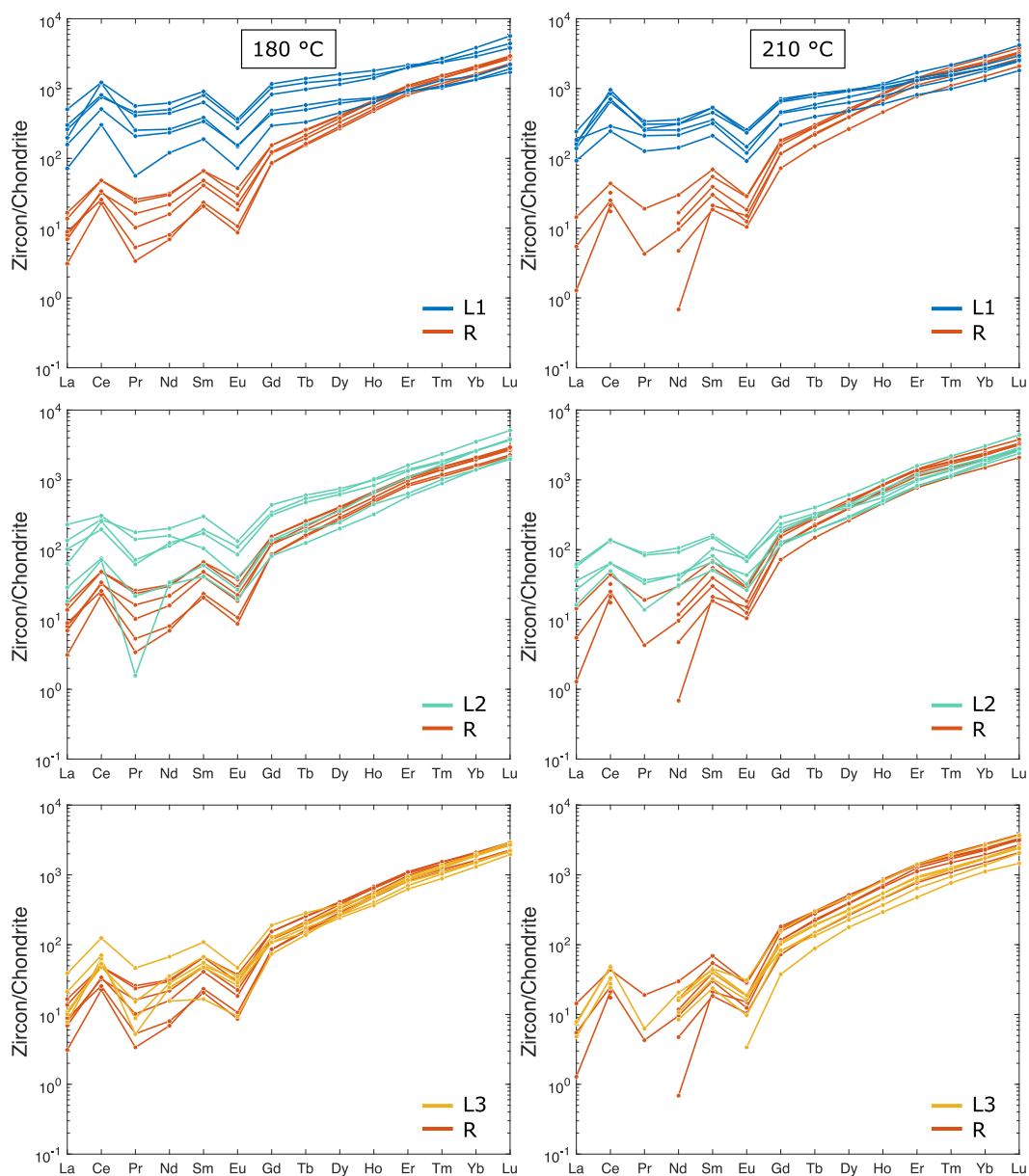
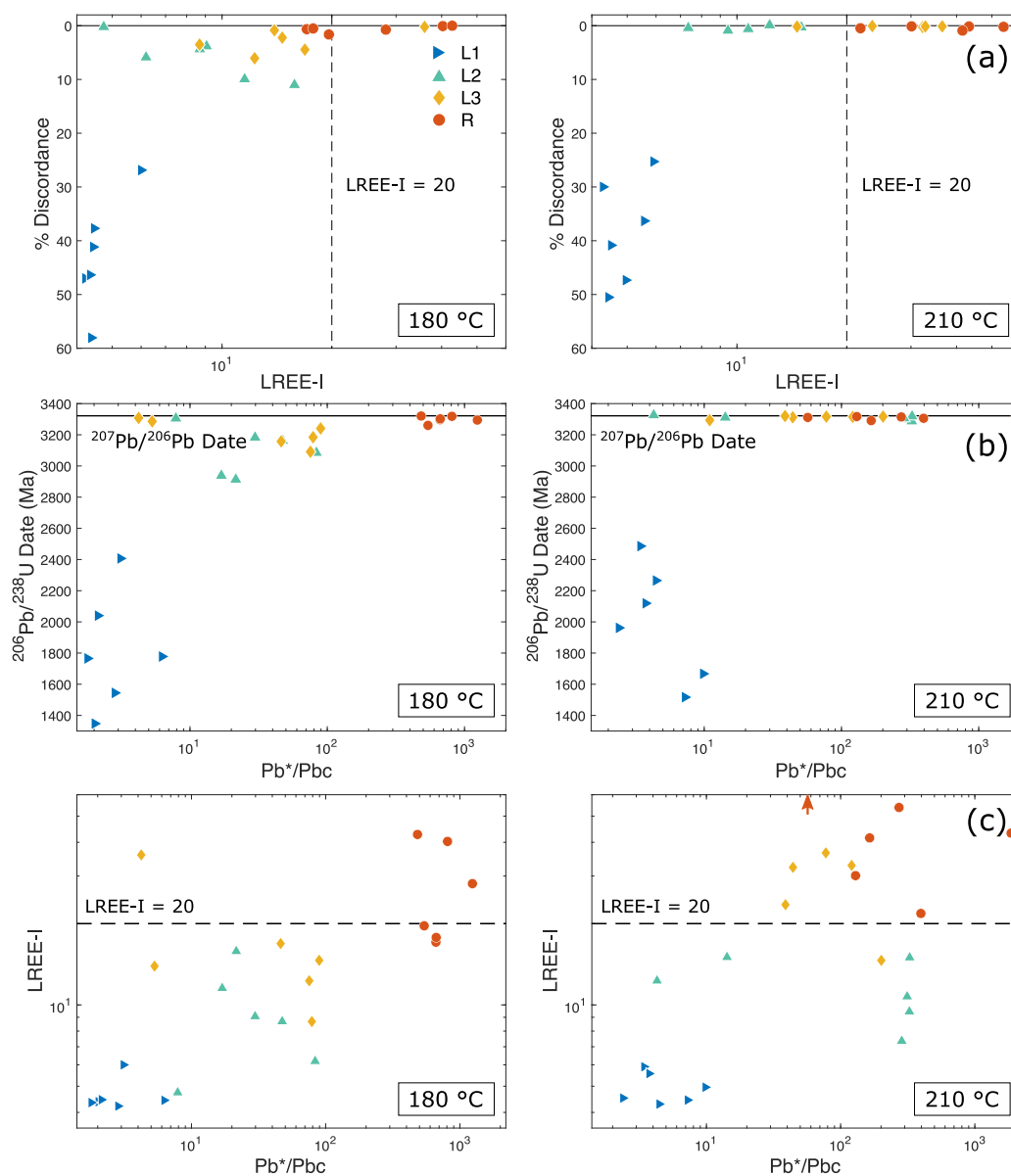


Figure 7. Chondrite-normalized REE spider diagrams for the 180 °C (left) and 210 °C (right) SAM-47 experiments comparing results for leachates and residues.

311 also evident in L1 and some L2 leachates from the 210 °C dataset, whereas most L3 leachates  
312 have compositions comparable to residues. Although a few leachates from the 210 °C  
313 experiment are relatively enriched in U, many have U compositions similar to residues.  
314



315 Figure 8. SAM-47 U-Pb and trace element data for the 180 °C (left) and 210 °C (right) experiments. **(a)** LREE-I versus  
 316 percent discordance. The horizontal solid line represents perfect concordance. The vertical dashed line depicts a  
 317 LREE-I threshold value of 20 below which data is notably more discordant. **(b)**  $^{206}\text{Pb}/^{238}\text{U}$  date plotted as a function  
 318 of the radiogenic  $\text{Pb}^*$  to common Pb ratio. Error bars for the percent discordant and  $^{206}\text{Pb}/^{238}\text{U}$  data reflect  
 319 propagated  $2\sigma$  analytical uncertainties. Most error bars are smaller than data markers. **(c)** The radiogenic  $\text{Pb}^*$  to  
 320 common Pb ratio versus the LREE-I showing a positive correlation between the two variables.  
 321



322 **3.3 KR18-04**

323

324 **3.3.1 Geologic setting and sample description**

325

326 KR18-04 zircons come from a Neoproterozoic rhyolite body associated with the glaciolacustrine  
327 Konnarock Formation in the Blue Ridge Mountains of Virginia, USA (MacLennan et al., 2020)  
328 (36°41'47.95", 81°24'22.08"). The Konnarock Formation is part of a structurally continuous  
329 sedimentary sequence deposited in a continental rift environment (Merschhat et al., 2014). This  
330 sequence unconformably overlies gneisses that are related to the Mesoproterozoic Grenville  
331 orogeny. ID-TIMS U-Pb ages for zircon separated from KR18-04 were used to show that glacial  
332 sedimentation was occurring at tropical latitudes at ~751 Ma, 30 million years prior to the  
333 Sturtian Snowball Earth (MacLennan et al., 2020). The post-depositional history of the region is  
334 complex and poorly resolved (Roden, 1991). Zircon fission track dates ( $T_c = \sim 205^\circ\text{C}$ ) from the  
335 Blue Ridge are variably reset by burial reheating and range in age from ~617 Ma to late  
336 Paleozoic dates (Naeser et al., 2016). Zircon (U-Th)/He dates ( $T_c = \sim 180^\circ\text{C}$  for crystalline zircon)  
337 from the Blue Ridge are contemporaneous with the late-stages of the Alleghenian orogeny  
338 indicating that the zircon He chronometer was fully reset by burial reheating and records  
339 synorogenic exhumation (Basler et al., 2021).

340

341 The KR18-04 rhyolite is crystal-rich with prominent, dominantly euhedral K-feldspar and quartz  
342 phenocrysts (MacLennan et al., 2020). Zircon grains separated from KR18-04 are euhedral, pink-  
343 orange, transparent, and minimally included. Grains exhibit concentric zoning in  
344 cathodoluminescent images with some faint, broad growth zones (McKanna et al., 2023).  
345 Raman data suggest that grains have accumulated low-to-intermediate radiation damage  
346 densities with equivalent alpha doses ranging from  $5 \times 10^{16}$  to  $2 \times 10^{17}$   $\alpha/\text{g}$  (McKanna et al., 2023).

347

348 **3.3.2 Previous geochronology**

349

350 Twelve single-crystal zircon ID-TIMS U-Pb analyses for KR18-04 are presented by MacLennan et  
351 al., (2020). Zircon were initially chemically abraded at 185 °C for 12 h. However, since many of  
352 these analyses retained significant Pb loss, the intensity of chemical abrasion was increased to  
353 210 °C for up to 14 h for the remaining samples. The twelve reported  $^{206}\text{Pb}/^{238}\text{U}$  dates – which  
354 combine both leaching conditions – range from  $753.08 \pm 0.33$  to  $741.21 \pm 0.35$  Ma. The  
355 reported data are statistically over-dispersed for a single population. The authors attribute the  
356 spread in ages along Concordia and the one discordant analysis to residual Pb loss (their Fig.  
357 S10). The reported eruption age for the sample derived from the eight oldest analyses and  
358 determined using a Bayesian Markov Chain Monte Carlo technique is  $752.60 \pm 0.12/-0.65$  Ma.

359

360 **3.3.3 U-Pb and trace element results**

361

362 ID-TIMS U-Pb results for KR18-04 samples are presented in Fig. 9 and Table S5. L1 leachates  
363 from both sample sets are affected by Pb loss; L1 leachates with  $\text{Pb}^*/\text{Pb}_c$  ratios  $>1$  are normally  
364 discordant and  $>150$  Ma younger than zircon residues. The lower intercept value for L1  
365 leachates from the 210 °C experiment suggests zero-age Pb-loss. L2 leachates from both

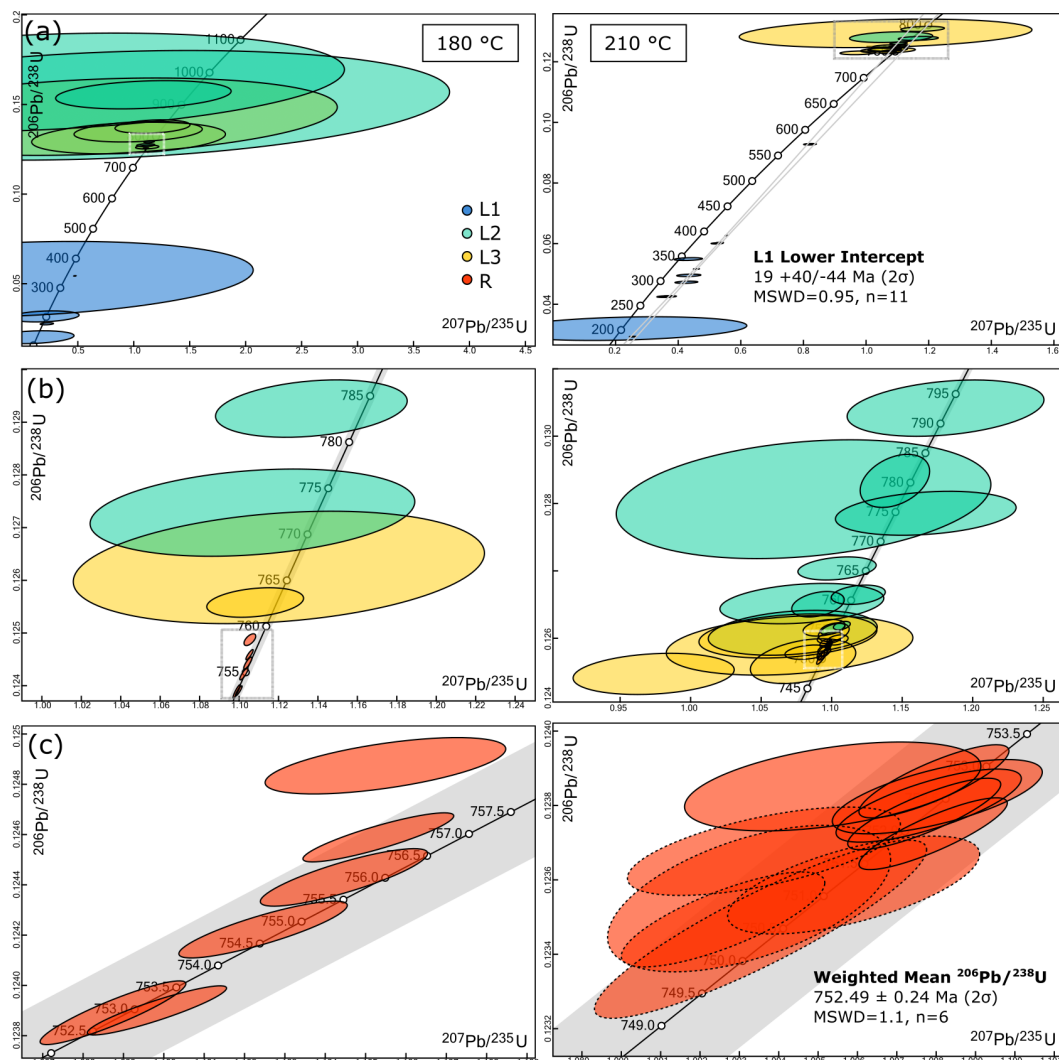
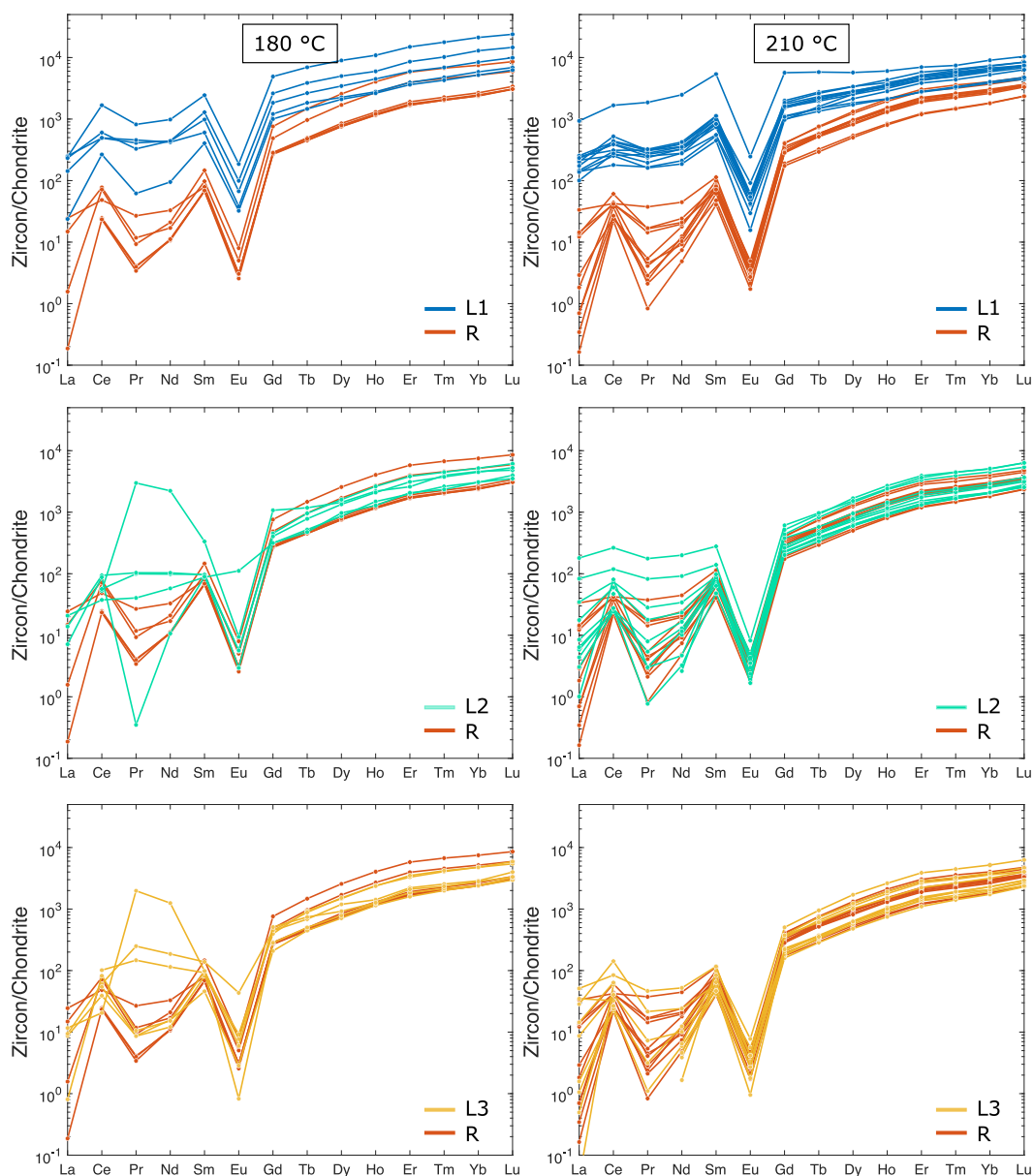


Figure 9. U-Pb concordia diagrams for the KR18-04 180 °C (left) and 210 °C (right) step-leaching experiments. (a) All data are depicted. (b) Close up of L2, L3, and R data excluding leachates with  $Pb^*/Pb_c$  values  $< 1$ . (c) Close up of zircon residues. The weighted mean  $^{206}Pb/^{238}U$  date reported for the 210 °C experiment includes residue data with solid ellipse borders. Ellipses with dashed borders were excluded due to low-quality U measurements. All ellipses reflect  $2\sigma$  analytical uncertainties.

366  
 367  
 368  
 369  
 370  
 371  
 372  
 373  
 374  
 375  
 376

from the 210 °C experiment form a tight cluster with a weighted mean  $^{206}Pb/^{238}U$  age of  $752.49 \pm 0.24$  Ma (MSWD = 1.1, n=6) in agreement with previous geochronology (MacLennan et al., 2020). This weighted-mean age includes analyses measured on the ATONA which produced more precise U measurements for these low-U zircon. The two 210 °C zircon aliquots that followed slightly different step-leaching protocols as outlined in Methods generated equivalent results.



377 Figure 10. Chondrite-normalized REE spider diagrams for the 180 °C (left) and 210 °C (right) KR18-04 experiments  
378 comparing results for leachates and residues.

379 in U, while L2 leachates are mildly enriched in U. L3 leachates have U compositions that are  
380 similar to residues (Fig. 5). L1 and some L2 leachates from the 210 °C experiment are enriched  
381 in LREEs relative to zircon residues, whereas L3 leachates have REE compositions similar to  
382 residues. All 210 °C leachates have low  $Pb^*/Pb_c$  ratios compared to residues. L1 leachates are

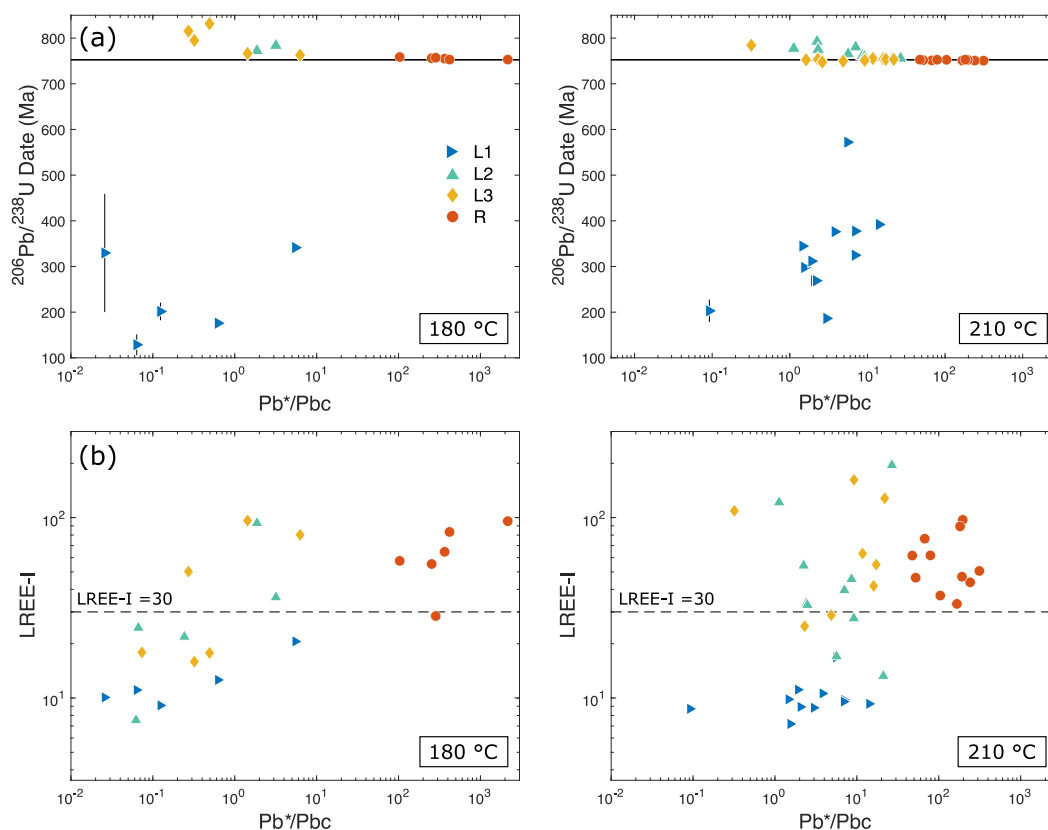


Figure 11. KR18-04 U-Pb and trace element data for the 180 °C (left) and 210 °C (right) experiments. **(a)**  $^{206}\text{Pb}/^{238}\text{U}$  date plotted as a function of the radiogenic  $\text{Pb}^*$  to common Pb ratio. Error bars for the percent discordant and  $^{206}\text{Pb}/^{238}\text{U}$  data reflect propagated  $2\sigma$  analytical uncertainties. Most error bars are smaller than data markers. **(b)** The radiogenic  $\text{Pb}^*$  to common Pb ratio versus the LREE-I.

383  
384  
385

Only ~10 to 15 % of KR18-04 zircon mass dissolved during step-leaching at 180 °C, leaving ~85 to 95 % of the zircon residue available for final isotopic analysis. At 210 °C, ~10 % to 30 % of the zircon dissolved during step-leaching, resulting in residue volumes of 70 to 90 %. Percent  $\text{Pb}^*$  mirrors results for percent zircon dissolved in both experiments.

390

#### 391 4. Discussion

392

##### 393 4.1 Reverse discordance

394

Reverse discordance and concordant analyses that are older than the samples' interpreted crystallization ages are common in the AS3 and KR18-04 datasets but absent in SAM-47. Concordant analyses that are "too old" can result from either minor U loss or  $\text{Pb}^*$  gain, causing datasets to lie along a discordia line that overlies the Concordia curve; for brevity, we will also refer to these analyses as "reversely discordant." Reverse discordance is most common in L2 and L3 leachates, however, a subset of residues from the AS3 and KR18-04 180 °C experiments

400



401 are also reversely discordant. Three L2 leachates for the Hadean zircon analyzed by Keller et al.,  
402 (2019) are similarly reversely discordant.

403

404 Reverse discordance in zircon stepwise dissolution experiments is generally attributed to  
405 leaching-induced experimental artefacts. Early step-leaching efforts yielded U-Pb isotopic  
406 variations that swung wildly between normally and reversely discordant from step-to-step  
407 (Todt and Büsch, 1981). Mattinson (1994, 2011) later attributed this effect to the authors'  
408 specific dissolution and spiking method which caused U and Pb to fractionate between  
409 supernate and U-bearing fluoride precipitates. However, later step-leaching experiments using  
410 different experimental procedures also exhibited reverse discordance in early leaching steps  
411 (Chen et al., 2001; Mattinson, 2005, 2011). Mattinson (2005, 2011) charged that early leaching  
412 steps must reflect a mixture of U and Pb from the higher-U dissolved zircon volume plus excess  
413 Pb\* leached from the lower-U intact zircon residue. Mattinson (2005, 2011) further  
414 demonstrated that annealing samples at temperatures between 800 - 1100 °C prior to chemical  
415 abrasion helped to minimize – but not eliminate – leaching-induced artefacts.

416

417 Reverse discordance is observed naturally in some untreated zircon (Kusiak et al., 2015;  
418 Wiemer et al., 2017; Williams et al., 1984). In such cases, reverse discordance is generally  
419 attributed to either the internal redistribution of Pb within a crystal or by external factors such  
420 as alteration by hydrothermal fluids (Mattinson et al., 1996). Alpha recoil can displace Pb\* from  
421 the position of its parent radioisotope by ~30 nm (Ewing et al., 2003; Weber, 1990, 1993). In  
422 crystals with fine-scale growth zoning, Pb\* produced by a U atom within a high-U zone can be  
423 implanted into a nearby low-U zone producing a localized occurrence of excess Pb\* in the low-  
424 U zone (Mattinson et al., 1996). Further, ion imaging and atom probe tomography studies of  
425 zircon support the case for nano-to-micro scale Pb redistribution under elevated temperatures  
426 and pressures (Kusiak et al., 2015; Peterman et al., 2019, 2021; Reddy et al., 2016). These  
427 studies show that unsupported Pb\* often forms clusters that are not spatially associated with  
428 parent radionuclide growth patterns. However, the exact mechanisms by which Pb\* migrates  
429 through the zircon structure are poorly understood.

430

431 Notably, our SAM-47 zircon does not exhibit reverse discordance suggesting that only some  
432 samples are predisposed to leaching-induced artifacts or leaching-exposed natural U-Pb  
433 fractionation. A zircon's U-Pb systematics as revealed by stepwise dissolution must therefore  
434 reflect its unique compositional characteristics such as the length-scale and magnitude of  
435 radionuclide zonation, the extent of Pb loss, or the sample's geological history. AS3 is  
436 hydrothermally altered, so a component of the reverse discordance observed could potentially  
437 reflect the redistribution of Pb isotopes during hydrothermal alteration (Takehara et al., 2018).  
438 Why KR18-04 zircon is susceptible to reverse discordance is less clear. Grains appear unaltered  
439 and most compositional zones are broad; however, some grains do have thin, high-U zones that  
440 could contribute to the internal redistribution of Pb\* (McKanna et al., 2023 their Fig. 4 & 15a).  
441 Zircon fission track and (U-Th)/He data from Blue Ridge indicate that the region was thermally  
442 affected by burial reheating during the late-Paleozoic Alleghenian Orogeny (Naeser et al., 2016;  
443 Roden, 1991). Still, there is no evidence that KR18-04 has experienced an extreme high-

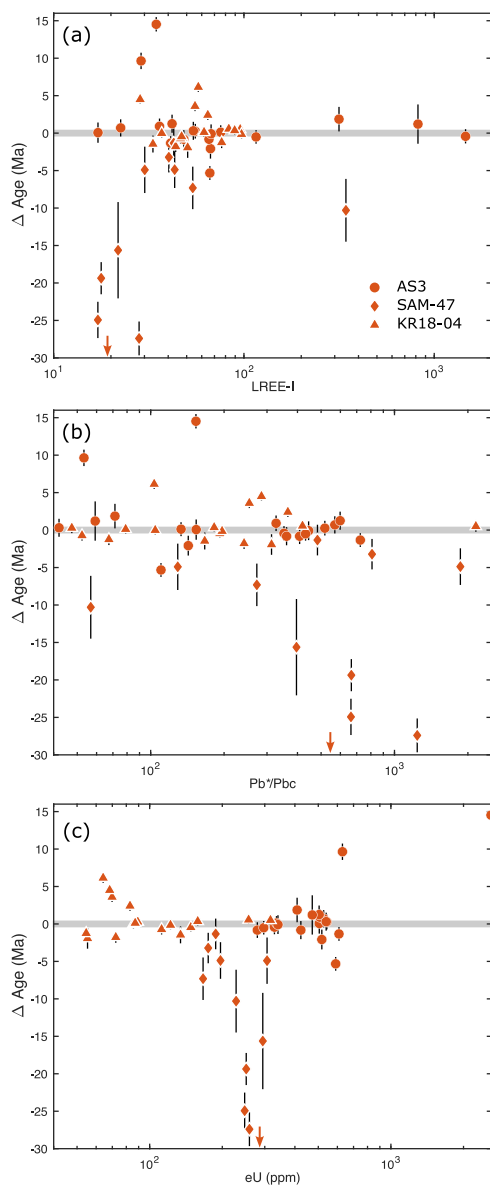


Figure 12. Trace element and Pb isotopic composition of zircon residues plotted against  $\Delta$  Age as described in text. The gray bar at  $\Delta$  Age = 0 Ma marks the accepted crystallization age for each zircon sample. The data portrayed is inclusive of residues from both the 180 °C and 210 °C experiments. **(a)** LREE-I versus the  $\Delta$  Age. **(b)**  $Pb^*/Pbc$  versus the  $\Delta$  Age. **(c)** eU versus  $\Delta$  Age. The arrow in each plot marks the placement of a datapoint from the SAM-47 dataset that plots at  $\Delta$  Age = -60 Ma.

444 temperature deformation event. SAM-47 may lack leaching-induced reverse discordance simply  
445 because Pb loss in the sample is so pervasive.  
446



447 Regardless of the underpinning causes of reverse discordance, this work and that of Mattinson  
448 (2005, 2011) demonstrate that increasing the leaching duration and/or temperature helps to  
449 eliminate zircon domains affected by open system behavior. These results also highlight that  
450 under-leaching samples can produce over-dispersed U-Pb datasets fraught with geologically  
451 meaningless analyses. Without the additional context that the 210 °C experiment provides, a  
452 researcher could easily interpret the older concordant dates from the 180 °C KR18-04 dataset,  
453 for example, as inheritance or prolonged magmatic residence. We stress, however, that our  
454 step-wise experiments are under-leached compared to the normal 12 h leaching step used in  
455 most labs (see Section 4.3).

456

#### 457 **4.2 The strengths and limitations of geochemical tools for identifying open-system behavior**

458

459 Common Pb and LREEs are incompatible in zircon. Mineral and melt inclusions and  
460 hydrothermally altered or metamict zones, however, tend to be enriched in LREEs and common  
461 Pb (Bell et al., 2016, 2019). Consequently, geochemical indicators such as a sample's LREE-index  
462 ( $LREE-I = [Dy]/[Nd] + [Dy]/[Sm]$ ) and  $Pb^*/Pb_c$  (provided demonstrably low laboratory blanks) are  
463 useful tools for identifying contamination, hydrothermal alteration, and metamictization.  
464 Indeed, our data show that the two variables are generally positively correlated (Fig. 4C, 8C,  
465 and 11B). Another important geochemical indicator is U concentration – or effective U  
466 concentration ( $eU = U + 0.235 \times Th$ ) – which is a measure of the relative radiation damage in a  
467 sample; zircon crystals or leachates from the same sample with higher eU have more radiation  
468 damage than crystals or leachates with lower eU.

469

470 These three geochemical indicators are useful tools for evaluating zircon dissolution. In the 180  
471 °C experiments, L1, L2, and some L3 leachates are enriched in LREE,  $Pb_c$ , and U relative to zircon  
472 residues. Whereas in the 210 °C experiments, L1 and some L2 leachates are enriched in the  
473 three variables, however, some L2 and most L3 leachates have compositions similar to residues.

474

475 Micro-X-ray computed tomography data presented by McKanna et al., (2023) for AS3 and SAM-  
476 47 zircon show that acid readily accesses crystal cores via fractures to dissolve mineral and melt  
477 inclusions and strongly metamict zones during L1 at 180 °C and 210 °C. As such, we interpret  
478 the LREE,  $Pb_c$ , and U enrichment in L1 leachates to reflect the dissolution of inclusions,  
479 metamict material, and – in the case of AS3 – hydrothermally altered zones. We attribute LREE,  
480  $Pb_c$ , and U enrichments in later leaching steps to the continued dissolution of soluble radiation-  
481 damaged or altered domains. KR18-04 zircon grains are more crystalline and typically lack  
482 fractures. Consequently, acid only accesses the cores of some grains, and some inclusions  
483 armored by highly crystalline material appear to survive twelve hours of chemical abrasion at  
484 180 °C or 210 °C (McKanna et al., 2023). Consequently, LREE and  $Pb_c$  enrichment in L2 and L3  
485 leaching steps could reflect later-stage dissolution of inclusions as well as the continued  
486 dissolution of radiation-damaged or altered domains.

487

488 Comparing leachate and residue chemistry is extremely effective at illuminating the progress of  
489 zircon dissolution. However, stepwise chemical abrasion is a time- and labor-intensive process.  
490 The overwhelming majority of zircon ID-TIMS U-Pb studies perform single-step chemical



491 abrasion and discard the leachate. Only the residue is characterized. In an ideal scenario,  
492 geochemical indicators such as those described here could be used to support the inclusion or  
493 exclusion of anomalously young (or old) analyses in geochronological interpretations. Fig. 12  
494 shows  $\Delta\text{Age}$  (Ma) of residues plotted as a function of a grain's LREE-I,  $\text{Pb}^*/\text{Pb}_c$ , or eU.  $\Delta\text{Age}$  is  
495 calculated as the difference between a residue's measured  $^{206}\text{Pb}/^{238}\text{U}$  date and each sample's  
496 accepted crystallization age. Negative values for  $\Delta\text{Age}$  reflect Pb loss, while positive values  
497 indicate reverse discordance.

498

499 Unfortunately, there is no clear correlation between either of the three geochemical indicators  
500 and  $\Delta\text{Age}$  in the samples analyzed. Instead, the data suggest that relative enrichments in LREE,  
501  $\text{Pb}_c$ , and U in residues are not reliable indicators of residual open system behavior. We  
502 speculate that the residual zircon affected by open-system behavior is likely volumetrically  
503 small compared to the volume of the residual closed-system zircon. Thus, the geochemical  
504 signature of the open-system behavior is likely masked by the bulk chemistry of the closed-  
505 system residue. Relative enrichments in LREE,  $\text{Pb}_c$ , and U in residues are likely useful  
506 geochemical indicators only if the residual open-system material is proportionally large.

507

#### 508 **4.3 Leaching temperature and one-step versus stepwise chemical abrasion**

509

510 Stepwise dissolution at 210 °C out-performed stepwise dissolution at 180 °C for all three zircon  
511 samples and produced more consistent, concordant datasets. Leaching at 210 °C dissolved  
512 zircon material affected by open-system behavior earlier in the leaching process minimizing the  
513 frequency and magnitude of normal and reverse discordance compared to the 180 °C  
514 experiments (Figures 1, 2, 6, 7, and 10). The efficacy of the hotter leaching temperature is also  
515 evident in zircon geochemistry; leaching at 210 °C more efficiently removed zircon material  
516 enriched in U, LREE, and  $\text{Pb}_c$ .

517

518 Notably, U-Pb results for AS3 and KR18-04 residues treated by stepwise dissolution at 180 °C  
519 are markedly worse than previous studies (MacLennan et al., 2020; Schoene et al., 2006).  
520 Chemical abrasion of AS3 zircon for 12 to 14 h at 180 °C by Schoene et al., (2006) produced  
521 concordant, statistically significant weighted mean U-Pb ages without signs of residual Pb loss  
522 or reverse discordance. Those authors used intense frantzing to target unincluded, diamagnetic  
523 zircon, whereas this study included altered grains. While some KR18-04 grains treated at 185 °C  
524 for 12 h by (MacLennan et al., 2020) exhibited Pb loss, none of their chemically abraded  
525 residues were found to be anomalously old or reversely discordant.

526

527 These apparent discrepancies beg the question: is a single 12 h leaching step is equivalent to  
528 stepwise dissolution in three 4 h leaching steps? PTFE has a low thermal conductivity making it  
529 an effective insulator. To evaluate how temperature in the PTFE-lined Parr pressure dissolution  
530 vessel changes with time, a small hole was drilled through the top of an old PTFE liner. The  
531 pressure vessel was assembled as normal minus the rupture and corrosion disks. A type-K  
532 thermocouple with an insulated wire was threaded through the top of the pressure vessel and  
533 into the center of the PTFE liner. The pressure vessel was then placed in a box furnace at 180 °C

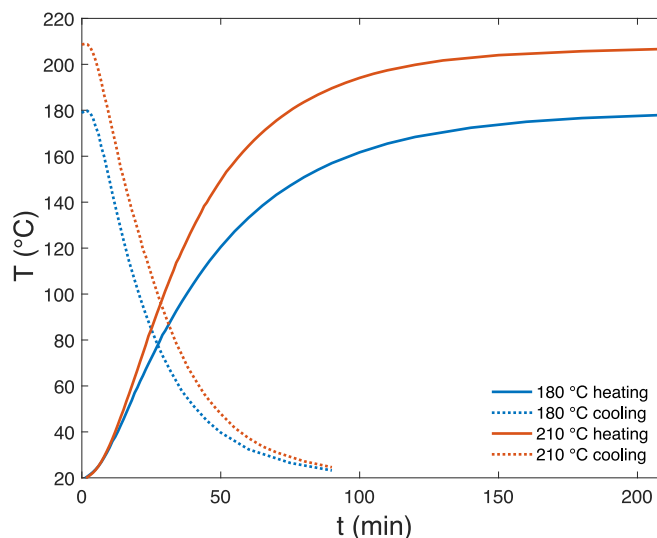


Figure 13. Temperature of the PTFE-lined pressure dissolution vessel plotted as a function of time. A fan was used to speed up cooling.

534 or 210 °C. Temperature was monitored using a Perfect Prime thermocouple thermometer until  
535 the temperature in the liner reached equilibrium with the box furnace. The pressure vessel was  
536 then removed from the furnace and placed in front of a fan, and temperature was recorded as  
537 the pressure vessel cooled to near room temperature.

538  
539 Results indicate that PTFE is indeed a very effective insulator; the interior of the pressure vessel  
540 heats and cools slowly (Fig. 13). It takes 90 to 95 minutes for the interior of the pressure vessel  
541 to reach within 20 °C of the target temperature and an additional 30 to 35 minutes to reach  
542 within 10 °C of the target temperature. The pressure vessel takes ~90 minutes to cool to room  
543 temperature once removed from the oven.

544  
545 Given the heating ramp up and cool down times for the PTFE-lined pressure dissolution vessel,  
546 samples spend only ~2 h of the 4 h leaching step within 10 °C of the target temperature. As  
547 such, a sample leached for 12 h in three consecutive 4 h steps spends ~6 h within 10 °C of the  
548 target temperature. Conversely, a sample leached in a single 12 h step spends ~10 h within 10  
549 °C of the target leaching temperature – ~4 h longer than the step-leached sample. Volume loss  
550 estimates for KR18-04 further support this conclusion; estimated volume losses for stepwise  
551 chemical abrasion (Figure 5) are generally lower than the estimated volume losses presented by  
552 McKanna et al., (2023; their Fig. 18) for zircon from the same sample aliquot that were  
553 chemically abraded for a single 12-h step.

554  
555 On the basis of the 10 °C threshold, we estimate that our dated residues have been leached for  
556 a duration equivalent to a single ~8 h leaching step. Given our U-Pb results, we conclude that  
557 zircon chemically abraded at 180 °C for a single 8 h step are “undercooked” and will likely



558 produce data affected by residual Pb loss and/or leaching-induced artifacts. Zircon samples  
 559 chemically abraded at 210 °C for a single 8-h leach are more likely to produce geologically  
 560 meaningful results. Unfortunately, we therefore cannot comment on the efficacy of the  
 561 routinely practiced 12-hour leaching at 180 °C used in many labs, except to say it is likely more  
 562 effective than the results for residues we present here.

563

564 **4.4 The relationships between alpha dose, Pb loss, and zircon dissolution: Moving toward a**  
 565 **more predictable model for chemical abrasion**

566

567 Zircon is an outstanding chronometer because radiogenic Pb is immobile in well crystalline  
 568 zircon (Cherniak et al., 2009; Cherniak and Watson, 2000). Establishing the alpha dose at which  
 569 radiogenic Pb can mobilize within the zircon structure would help make Pb loss more  
 570 predictable. We calculate three different time-integrated alpha doses for each sample using the  
 571 radionuclide concentrations determined for leachates and residues (Table 1). “Total” alpha  
 572 dose assumes a damage accumulation interval equivalent to a sample’s crystallization age. This  
 573 calculation ignores the possibility of radiation damage annealing. “Present day” alpha dose  
 574 estimates attempt to take geological annealing into account. Radiation damage anneals at  
 575 temperatures above ~200 to 300°C on geological timescales (Bernet, 2009; Yamada et al.,  
 576 2007). The closure temperature for the (U-Th)/He system in crystalline zircon is ~180 °C  
 577 (Guenther et al., 2013; Reiners et al., 2004). As such, we use published zircon (U-Th)/He dates  
 578 or thermal histories derived from zircon (U-Th)/He datasets for the Minnesota River Valley  
 579

580 (Guenther et al., 2013; McDannell et al., 2022), the Eastern Pilbara craton (Magee et al.,  
 581 2017), and the Virginia Blue Ridge (Basler et al., 2021) to estimate minimum damage  
 582 accumulation intervals for samples’ “present day” alpha doses. Since zircon (U-Th)/He dates for  
 583 the Eastern Pilbara craton broadly overlap the lower-intercept U-Pb Concordia age for SAM-47,  
 584 we take the lower-intercept age as the damage accumulation interval. Chosen intervals for AS3,  
 585 SAM-47, and KR18-04 are 750 Ma, 751 Ma, and 298 Ma, respectively.

586

587 “Present day” alpha dose estimates can also be established independently using Raman  
 588 spectroscopy, since key bands in the zircon Raman spectrum broaden predictably with

Table 1. Alpha dose estimates.

Sample	$\alpha$ dose ( $\alpha/g$ ) <sup>1</sup>						$\alpha_r$ dose ( $\alpha/g$ ) <sup>2</sup>	
	Total		Pb Loss		Present Day		Present Day	
	Min	Max	Min	Max	Min	Max	Min	Max
AS3	$4 \times 10^{17}$	$1 \times 10^{20}$	$3 \times 10^{17}$	$8 \times 10^{19}$	$3 \times 10^{17}$	$8 \times 10^{19}$	$2 \times 10^{17}$	$>1 \times 10^{19}$
SAM-47	$2 \times 10^{18}$	$1 \times 10^{19}$	$1 \times 10^{18}$	$8 \times 10^{18}$	$3 \times 10^{17}$	$2 \times 10^{18}$	$6 \times 10^{17}$	$2 \times 10^{18}$
KR18-04	$1 \times 10^{17}$	$1 \times 10^{19}$	$4 \times 10^{16}$	$4 \times 10^{18}$	$4 \times 10^{16}$	$4 \times 10^{18}$	$5 \times 10^{16}$	$7 \times 10^{17}$

<sup>1</sup>Calculated using measured U and Th concentrations and damage accumulation intervals as described in text.

<sup>2</sup>Raman-based alpha dose estimates reported by McKanna et al., (2023).

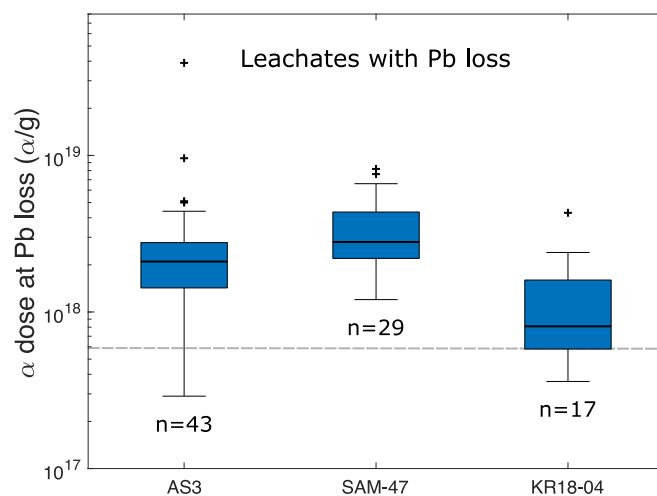


Figure 14. Box plot diagram showing alpha dose distribution for leachates (L1, L2, and L3) affected by Pb loss. Data include both the 180 °C and 210 °C experiments. The gray dashed line highlights our best estimate for the minimum alpha dose required for Pb loss to occur. Each box shows the median value (black bar), the upper and lower quartiles (box), the minimum and maximum values (whiskers), and statistical outliers (plus marks).

589 increasing alpha dose (Nasdala et al., 2001; Palenik et al., 2003). “Present day” alpha doses for  
590 AS3 and SAM-47 closely match Raman-based alpha doses ( $\alpha_r$ ) determined by (McKanna et al.,  
591 2023) for zircon from the same sample aliquots (Table 1). “Present day” alpha doses for KR18-  
592 04 have a similar lower bound but a higher upper bound compared to Raman estimates. Most  
593 likely, Raman measurements failed to capture volumetrically small, higher-U domains such as  
594 the thin concentric dissolution features evident in secondary electron images of KR18-04  
595 residues (McKanna et al., 2023, their Fig. 15a-I reproduced here in Fig. 16b).

596

597 The final calculation estimates alpha dose at the time of Pb loss. Because AS3 and KR18-04  
598 exhibit zero-age Pb-loss discords, “present day” and “Pb loss” alpha doses estimates are  
599 equivalent. The Pb-loss discord for SAM-47, however, suggests that Pb loss occurred in the  
600 distant geological past at or before  $751 \pm 140$  Ma (Fig. 6C). Therefore, the maximum “Pb loss”  
601 damage accumulation interval is the difference between the sample’s upper and lower  
602 intercept ages which equates to  $\sim 2571$  Ma.

603

604 Fig. 14 shows the distribution of “Pb loss” alpha dose estimates for all leachates affected by Pb  
605 loss. Despite vastly different geological settings and ranges in radiation damage densities,  
606 leachates affected by Pb loss exhibit similar alpha dose distributions. The majority have alpha  
607 doses that are  $\geq 6 \times 10^{17}$   $\alpha/g$ . We therefore establish this alpha dose as our best estimate for  
608 the threshold above which Pb can mobilize within the zircon structure. Notably, this threshold  
609 is somewhat lower than the alpha dose –  $1 \times 10^{18}$   $\alpha/g$  – at which zircon material properties such  
610 as density begin to change (Ewing et al., 2003; Nasdala et al., 2004). However, the  $6 \times 10^{17}$   $\alpha/g$   
611 threshold is similar to some estimates for the alpha dose at which helium diffusion kinetics

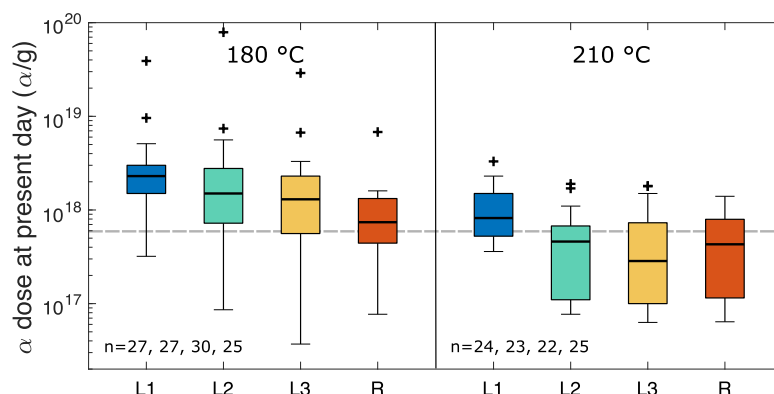


Figure 15. Box plot diagram showing present day alpha dose distributions at each step of zircon dissolution. Data includes all AS3, SAM-47 and KR18-04 leachates and residues. Alpha dose estimates reflect samples' present day radiation damage. The gray dashed line highlights our best estimate for the minimum alpha dose required for Pb loss to occur. Each box shows the median value (black bar), the upper and lower quartiles (box), the minimum and maximum values (whiskers), and statistical outliers (plus marks).

612 begin to increase causing the closure temperature for He in zircon to decrease (Anderson et al.,  
613 2017, 2020). The mechanism that causes Pb loss – diffusion, leaching, or recrystallization – is  
614 not clear.

615

616 For the best geochronological outcomes, chemical abrasion should target zircon material with  
617 alpha doses  $\geq 6 \times 10^{17}$   $\alpha/g$ . Fig. 15 shows “present day” alpha dose estimates for all leachates  
618 and residues from the 180 °C and 210 °C experiments. In the 180 °C experiments, the median  
619 alpha dose decreases with increasing leaching duration consistent with the expected effects of  
620 radiation damage on zircon solubility. A majority of residues from the 180 °C experiments have  
621 alpha doses  $> 6 \times 10^{17}$   $\alpha/g$  suggesting that residues may be affected by residual open system  
622 behavior in agreement with our U-Pb isotopic results. Evidently, dissolving zircon with lower  
623 alpha doses requires longer leaching durations at 180 °C than achieved in this study, which was  
624 equivalent to a single 8-hour leach step. In contrast, the median alpha dose for residues as well  
625 as L2 and L3 leachates from the 210 °C experiments have alpha doses below the established  
626 threshold. Zircon material with alpha doses  $\geq 6 \times 10^{17}$   $\alpha/g$  is thus readily dissolved at short  
627 leaching durations at 210 °C.

628

629 Framing Pb loss and zircon dissolution in terms of alpha dose better allows the user to tailor  
630 their chemical abrasion approach to a specific zircon dataset. Fig. 16 plots alpha dose as a  
631 function of time for different U concentrations. As described above, different time intervals can  
632 be selected for damage accumulation depending on the calculation's goal. This figure is a  
633 simple visual representation that can help a researcher determine whether or not a sample is  
634 likely to be affected by Pb loss. Chemical abrasion is a time-consuming method that is applied  
635 to the majority of ID-TIMS U-Pb datasets, but it may be unnecessary for low-alpha dose,  
636 inclusion-free zircon. Further, by estimating a sample's “present day” alpha dose distribution, a  
637 user can better predict how readily a sample will dissolve. For example, if a sample has a lot of

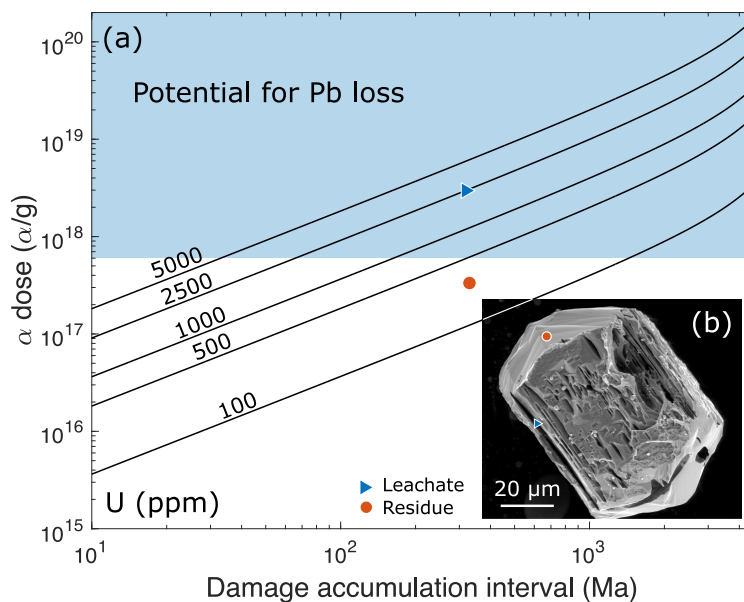


Figure 16. **(a)** Contour diagram showing alpha dose as a function of time for U concentrations ranging from 100 ppm to 5000 ppm. Calculations assume a fixed Th/U of 0.5 and no annealing. The shaded region highlights the alpha dose range in which Pb loss is most likely. **(b)** Secondary electron image of KR18-04 residue chemically abraded at 210 °C for 12 h from McKanna et al., (2023). The blue triangle marks a thin concentric zone that dissolved during chemical abrasion (leachate), while the red circle marks a portion of the zircon that remained intact (residue). Markers in b) correlate to markers in a) and illustrate how a grain with radionuclide zoning can have accumulated alpha doses above and below the threshold for Pb mobilization.

638 accumulated radiation damage like SAM-47, leaching longer than a single 8-h step at 210 °C will  
639 likely leave little to no residue for isotopic analysis. Whereas, if a sample has a lower alpha dose  
640 like KR18-04, a longer 210 °C leach is unlikely to have a significant effect.

641

642 As highlighted in Fig. 16b, perhaps the most persistent challenge when it comes to tailoring  
643 chemical abrasion for a specific zircon dataset or even a specific zircon crystal is radionuclide  
644 zoning. The spatial distribution of radionuclides and the magnitude of intracrystalline variations  
645 in radiation damage strongly affect the mechanics of zircon dissolution (McKanna et al., 2023).  
646 Radionuclide zoning explains the inconsistent dissolution behavior evidenced in Fig. 5. For  
647 example, the percent zircon dissolved in each leaching step decreases from L1 to L3 for AS3  
648 zircon, remains constant or decreases for SAM-47 zircon, and remains constant or increases for  
649 KR18-04 zircon. This non-pattern occurs because the percent zircon dissolved is not only a  
650 function of alpha dose, but also 1) the volumetric proportion of zircon with a given alpha dose,  
651 and 2) which portions of a crystal are in contact with HF at any given time during the leaching  
652 process. Building a comprehensive model for chemical abrasion will ultimately require both  
653 geochemical and textural inputs.

654

655

656



## 657 5. Conclusions

658

659 Single-crystal stepwise dissolution experiments performed at 180 °C and 210°C provide new  
660 insights into the geochronological and geochemical effects of chemical abrasion on zircon  
661 datasets. Because of the insulating properties of the PTFE-lined pressure dissolution vessel,  
662 stepwise dissolution in three 4-h leaching steps is not equivalent to a 12-h single-step chemical  
663 abrasion, the method most commonly used by the zircon ID-TIMS U-Pb community. We  
664 estimate that our stepwise dissolution approach is roughly equivalent to 8-h single-step  
665 chemical abrasion. Stepwise dissolution at 180 °C produced over-dispersed U-Pb datasets  
666 affected by both residual Pb-loss and leaching-induced or leaching-exposed artefacts which  
667 present as reverse discordance. Without the context of the 210 °C results, reverse discordance  
668 in the 180 °C datasets could easily be mistaken for prolonged crystallization or inheritance and  
669 lead to spurious geological interpretations. Longer leaching durations are likely needed to  
670 produce robust geochronological datasets at 180 °C.

671

672 Stepwise dissolution at 210 °C outperformed the 180 °C experiments by all measures for the  
673 three zircon samples analyzed producing more reproducible, concordant results. Ultimately,  
674 how a zircon sample responds to any chemical abrasion protocol will be sample-dependent.  
675 However, our results suggest that 8-h single-step chemical abrasion at 210 °C may be effective  
676 at mitigating Pb loss and reverse discordance for a wide range of zircon samples. Further study  
677 of different zircon samples is needed. Our results, however, clearly demonstrate that leaching  
678 durations longer than an 8-h single step are required for chemical abrasion at 180 °C to be  
679 effective.

680

681 U concentration,  $Pb^*/Pb_c$ , and LREE enrichment are useful tools for tracking the dissolution of  
682 inclusions and radiation-damaged or altered material during stepwise dissolution. These  
683 geochemical indicators, however, are not effective at identifying residual Pb loss in the zircon  
684 residues analyzed.

685

686 We attempted to constrain the relationship between Pb loss and radiation damage by  
687 calculating an alpha dose for each leachate based on its measured radionuclide concentration  
688 and an estimated damage accumulation interval informed by the sample's geologic history. "Pb  
689 loss" alpha dose estimates suggest that Pb may mobilize within the zircon structure at alpha  
690 doses as low as  $6 \times 10^{17}$   $\alpha/g$ . "Present day" alpha dose estimates indicate that many residues  
691 treated by stepwise dissolution at 180 °C have alpha doses above the  $6 \times 10^{17}$   $\alpha/g$  threshold,  
692 and consequently, many 180 °C residues are affected by residual Pb loss. The majority of  
693 residues treated at 210 °C – and many L2 and L3 leachates – have "present day" alpha doses  
694 below this threshold. Grains expected to have accumulated alpha doses  $< 6 \times 10^{17}$   $\alpha/g$  based on  
695 expected radionuclide concentrations and damage accumulation intervals are unlikely to be  
696 affected by Pb loss and may not require chemical abrasion. However, chemical abrasion may  
697 help improve the precision of U-Pb analyses even in low-damage grains by dissolving  $Pb_c$ -  
698 bearing inclusions. The effectiveness of any chemical abrasion protocol will ultimately be  
699 sample-dependent, since zircon dissolution depends not only on a grain's bulk chemistry, but  
700 also the spatial distribution and magnitude of intracrystalline variations in radiation damage.



701 **Data availability.** All data presented are included in this paper or the Supplement.

702 **Supplement.** The supplement related to this article is available online at:

703 **Author contributions.** AJM carried out the experiments and wrote the manuscript. All authors –  
704 AJM, DS, and BS – contributed to the experiment design and data reduction, interpretation, and  
705 presentation.

706 **Competing interests.** The contact author has declared that none of the authors has any  
707 competing interests.

708 **Disclaimer.** Publisher’s note: Copernicus Publications remains neutral with regard to  
709 jurisdictional claims in published maps and institutional affiliations.

710 **Acknowledgements.** Thank you to Mami Takehara of the National Institute of Polar Research in  
711 Tokyo, Japan, for providing the hydrothermally altered AS3 zircon crystals used in this study.

712 **Financial support.** This work was supported by research funds provided by the Department of  
713 Geosciences at Princeton University granted to Alyssa J. McKanna as part of her Harry Hess  
714 Postdoctoral Fellowship.

715 **Review statement.**

## 716 **References**

717

718 Anderson, A. J., Hodges, K. V., & van Soest, M. C. (2017). Empirical constraints on the effects of  
719 radiation damage on helium diffusion in zircon. *Geochimica et Cosmochimica Acta*, 218,  
720 308–322. <https://doi.org/10.1016/j.gca.2017.09.006>

721 Anderson, A. J., van Soest, M. C., Hodges, K. V., & Hanchar, J. M. (2020). Helium diffusion in  
722 zircon: Effects of anisotropy and radiation damage revealed by laser depth profiling.  
723 *Geochimica et Cosmochimica Acta*, 274, 45–62. <https://doi.org/10.1016/j.gca.2020.01.049>

724 Barley, M. E., & Pickard, A. L. (1999). 41-62 An extensive, crustally-derived. In *Precambrian*  
725 *Research* (Vol. 96).

726 Basler, L. C., Baughman, J. S., Fame, M. L., & Haproff, P. J. (2021). Spatially variable syn- and  
727 post-Alleghanian exhumation of the central Appalachian Mountains from zircon (U-Th)/He  
728 thermochronology. *Geosphere*, 17(4), 1151–1169. <https://doi.org/10.1130/GES02368.1>

729 Bell, E. A., Boehnke, P., Barboni, M., & Harrison, T. M. (2019). Tracking chemical alteration in  
730 magmatic zircon using rare earth element abundances. *Chemical Geology*, 510, 56–71.  
731 <https://doi.org/10.1016/j.chemgeo.2019.02.027>

732 Bell, E. A., Boehnke, P., & Harrison, T. M. (2016). Recovering the primary geochemistry of Jack  
733 Hills zircons through quantitative estimates of chemical alteration. *Geochimica et*  
734 *Cosmochimica Acta*, 191, 187–202. <https://doi.org/10.1016/j.gca.2016.07.016>

735 Bernet, M. (2009). A field-based estimate of the zircon fission-track closure temperature.  
736 *Chemical Geology*, 259(3–4), 181–189. <https://doi.org/10.1016/j.chemgeo.2008.10.043>



- 737 Bowring, J. F., McLean, N. M., & Bowring, S. A. (2011). Engineering cyber infrastructure for U-Pb  
738 geochronology: Tripoli and U-Pb-Redux. *Geochemistry, Geophysics, Geosystems*, 12(6).  
739 <https://doi.org/10.1029/2010GC003479>
- 740 Chen, F., Siebel, W., & Satir, M. (2001). Zircon U-Pb and Pb-isotope fractionation during  
741 stepwise HF acid leaching and geochronological implications. In *Chem. Geol* (Vol. 172).  
742 [www.elsevier.com/locate/chemgeo](http://www.elsevier.com/locate/chemgeo)
- 743 Cherniak, D. J., & Watson, E. B. (2000). Pb diffusion in zircon. *Chemical Geology*, 172, 5–24.  
744 [www.elsevier.com/locate/chemgeo](http://www.elsevier.com/locate/chemgeo)
- 745 Cherniak, D. J., Watson, E. B., & Thomas, J. B. (2009). Diffusion of helium in zircon and apatite.  
746 *Chemical Geology*, 268(1–2), 155–166. <https://doi.org/10.1016/j.chemgeo.2009.08.011>
- 747 Condon, D. J., Schoene, B., McLean, N. M., Bowring, S. A., & Parrish, R. R. (2015). Metrology and  
748 traceability of U-Pb isotope dilution geochronology (EARTHTIME Tracer Calibration Part I).  
749 *Geochimica et Cosmochimica Acta*, 164, 464–480.  
750 <https://doi.org/10.1016/j.gca.2015.05.026>
- 751 Corfu, F. (2013). A century of U-pb geochronology: The long quest towards concordance. In  
752 *Bulletin of the Geological Society of America* (Vol. 125, Issues 1–2, pp. 33–47).  
753 <https://doi.org/10.1130/B30698.1>
- 754 Davis, D. W., & Krogh, T. E. (2000). Preferential dissolution of <sup>234</sup>U and radiogenic Pb from a-  
755 recoil-damaged lattice sites in zircon: implications for thermal histories and Pb isotopic  
756 fractionation in the near surface environment. In *Chemical Geology* (Vol. 172).  
757 [www.elsevier.com/locate/chemgeo](http://www.elsevier.com/locate/chemgeo)
- 758 Ewing, R. C., Meldrum, A., Wang, L., Weber, W. J., & Corrales, L. R. (2003). Radiation Effects in  
759 Zircon. *Reviews in Mineralogy and Geochemistry*, 53(1), 387–425.  
760 <https://doi.org/10.2113/0530387>
- 761 Geisler, T., Pidgeon, R. T., van Bronswijk, W., & Kurtz, R. (2002). Transport of uranium, thorium,  
762 and lead in metamict zircon under low-temperature hydrothermal conditions. *Chemical*  
763 *Geology*, 191, 141–154. [www.elsevier.com/locate/chemgeo](http://www.elsevier.com/locate/chemgeo)
- 764 Gerstenberger, H., & Haase, G. (1997). A highly effective emitter substance for mass  
765 spectrometric Pb isotope ratio determinations. In *Chemical Geology* (Vol. 136).  
766 Guenthner, W. R., Reiners, P. W., Ketcham, R. A., Nasdala, L., & Giester, G. (2013). Helium  
767 diffusion in natural zircon: radiation damage, anisotropy, and the interpretation of zircon  
768 (U-TH)/He thermochronology. *American Journal of Science*, 313(3), 145–198.  
769 <https://doi.org/10.2475/03.2013.01>
- 770 Heiss, J., Condon, D. J., McLean, N., & Noble, S. R. (2012). <sup>238</sup>U/<sup>235</sup>U Systematics in Terrestrial  
771 Uranium-Bearing Minerals. *Science*, 335(6076), 1610–1613.
- 772 Huyskens, M. H., Zink, S., & Amelin, Y. (2016). Evaluation of temperature-time conditions for  
773 the chemical abrasion treatment of single zircons for U-Pb geochronology. *Chemical*  
774 *Geology*, 438, 25–35. <https://doi.org/10.1016/j.chemgeo.2016.05.013>
- 775 Jaffey, A. H., Flynn, K. F., Glendenin, L. E., Bentley, W. C., & Essling, A. M. (1971). Precision  
776 Measurement of Half-Lives and Specific Activities of <sup>235</sup>U and <sup>238</sup>U. *Physical Review C*,  
777 4(5), 1889–1906. <https://doi.org/10.1103/PhysRevC.4.1889>
- 778 Keller, B. (2023). Technical Note: Pb-loss-aware Eruption/Deposition Age Estimation. *GChron*,  
779 *Preprint*. <https://doi.org/10.5194/gchron-2023-9>



- 780 Keller, B. C., Boehnke, P., Schoene, B., & Harrison, T. M. (2019). Stepwise chemical abrasion-  
781 isotope dilution-thermal ionization mass spectrometry with trace element analysis of  
782 microfractured Hadean zircon. *Geochronology*, 1(1), 85–97.  
783 <https://doi.org/10.5194/gchron-1-85-2019>
- 784 Kloppenburg, A. (2003). *Structural evolution of the Marble Bar Domain, Pilbara granite-  
785 greenstone terrain, Australia : the role of Archaean mid-crustal detachments = Structurele  
786 evolutie van het Marble Bar Domein, Pilbara graniet-groensteen terrein, Australie : de rol  
787 van Archaeische decollements in de middenkorst* [PhD Dissertation]. Utrecht University.
- 788 Kloppenburg, A., White, S. H., & Zegers, T. E. (2001). Structural evolution of the Warrawoona  
789 Greenstone Belt and adjoining granitoid complexes, Pilbara Craton, Australia: implications  
790 for Archaean tectonic processes. In *Precambrian Research* (Vol. 112).  
791 [www.elsevier.com/locate/precamres](http://www.elsevier.com/locate/precamres)
- 792 Krogh, T. E. (1973). A low-contamination method for hydrothermal decomposition of zircon and  
793 extraction of U and Pb for isotopic age determinations. *Geochimica et Cosmochimica Acta*,  
794 37, 485–494.
- 795 Krogh, T. E. (1981). Improved accuracy of U-Pb zircon ages by the creation of more concordant  
796 systems using an air abrasion technique. *Geochimica et Cosmochimica Acta*, 46, 637–649.
- 797 Kusiak, M. A., Dunkley, D. J., Wirth, R., Whitehouse, M. J., Wilde, S. A., & Marquardt, K. (2015).  
798 Metallic lead nanospheres discovered in ancient zircons. *Proceedings of the National  
799 Academy of Sciences of the United States of America*, 112(16), 4958–4963.  
800 <https://doi.org/10.1073/pnas.1415264112>
- 801 MacLennan, S. A. (2019). *Temporal constraints on Archean crustal geodynamics and  
802 Neoproterozoic glaciation* [PhD Dissertation]. Princeton University.
- 803 MacLennan, S. A., Eddy, M. P., Merschat, A. J., Mehra, A. K., Crockford, P. W., Maloof, A. C.,  
804 Southworth, C. S., & Schoene, B. (2020). Geologic evidence for an icehouse Earth before  
805 the Sturtian global glaciation. *Science Advances*, 6(24).  
806 <https://doi.org/10.1126/sciadv.aay6647>
- 807 MacLennan, S. A., Eddy, M. P., Merschat, A. J., Mehra, A. K., Crockford, P. W., Maloof, A. C.,  
808 Southworth, C. S., & Schoene, B. (2020). *Geologic evidence for an icehouse Earth before  
809 the Sturtian global glaciation*. <http://advances.sciencemag.org/>
- 810 Magee, C. W., Danišik, M., & Mernagh, T. (2017). Extreme isotopologue disequilibrium in  
811 molecular SIMS species during SHRIMP geochronology. *Geoscientific Instrumentation,  
812 Methods and Data Systems*, 6(2), 523–536. <https://doi.org/10.5194/gi-6-523-2017>
- 813 Mattinson, J. M. (1994). Mineralogy and Petrology A study of complex discordance in zircons  
814 using step-wise dissolution techniques. *Contributions to Mineralogy and Petrology*, 116,  
815 117–129.
- 816 Mattinson, J. M. (2005). Zircon U-Pb chemical abrasion (“CA-TIMS”) method: Combined  
817 annealing and multi-step partial dissolution analysis for improved precision and accuracy  
818 of zircon ages. *Chemical Geology*, 220(1–2), 47–66.  
819 <https://doi.org/10.1016/j.chemgeo.2005.03.011>
- 820 Mattinson, J. M. (2011). Extending the Krogh legacy: development of the CA–TIMS method for  
821 zircon U–Pb geochronology This article is one of a series of papers published in this Special  
822 Issue on the theme of *Geochronology* in honour of Tom Krogh. *Canadian Journal of Earth  
823 Sciences*, 48(2), 95–105. <https://doi.org/10.1139/E10-023>



- 824 Mattinson, J. M., Graubard, C. M., Parkinson, D. L., & McClelland, W. C. (1996). U-Pb Reverse  
825 Discordance in Zircons: The Role of Fine-Scale Oscillatory Zoning and Sub-Micron Transport  
826 of Pb. In A. Basu & S. Hart (Eds.), *Earth Processes: Reading the Isotopic Code* (pp. 355–370).  
827 AGU. <https://doi.org/10.1029/GM095p0355>
- 828 McDannell, K. T., Keller, C. B., Guenther, W. R., Zeitler, P. K., & Shuster, D. L. (2022).  
829 Thermochronologic constraints on the origin of the Great Unconformity. *Proceedings of*  
830 *the National Academy of Sciences*, 119(5). <https://doi.org/10.1073/pnas.2118682119>
- 831 McKanna, A. J., Koran, I., Schoene, B., & Ketcham, R. A. (2023). Chemical abrasion: the  
832 mechanics of zircon dissolution. *Geochronology*, 5(1), 127–151.  
833 <https://doi.org/10.5194/gchron-5-127-2023>
- 834 McLean, N. M., Bowring, J. F., & Bowring, S. A. (2011). An algorithm for U-Pb isotope dilution  
835 data reduction and uncertainty propagation. *Geochemistry, Geophysics, Geosystems*,  
836 12(6). <https://doi.org/10.1029/2010GC003478>
- 837 McLean, N. M., Condon, D. J., Schoene, B., & Bowring, S. A. (2015). Evaluating uncertainties in  
838 the calibration of isotopic reference materials and multi-element isotopic tracers  
839 (EARTHTIME Tracer Calibration Part II). *Geochimica et Cosmochimica Acta*, 164, 481–501.  
840 <https://doi.org/10.1016/j.gca.2015.02.040>
- 841 Meldrum, A., Boatner, L. A., Weber, W. J., & Ewing, R. C. (1998). Radiation damage in zircon and  
842 monazite. *Geochimica et Cosmochimica Acta*, 62(14), 2509–2520.
- 843 Merschat, A. J., Southworth, S., McClellan, E., Tollo, R. P., Rankin, D. W., Hooper, S., & Bauer, S.  
844 (2014). Key structural and stratigraphic relationships from the northeast end of the  
845 Mountain City window and the Mount Rogers area, Virginia–North Carolina–Tennessee. In  
846 *Elevating Geoscience in the Southeastern United States: New Ideas about Old Terranes—*  
847 *Field Guides for the GSA Southeastern Section Meeting, Blacksburg, Virginia, 2014* (pp. 63–  
848 101). Geological Society of America. [https://doi.org/10.1130/2014.0035\(03\)](https://doi.org/10.1130/2014.0035(03))
- 849 Mezger, K., & Krogstad, E. J. (1997). Interpretation of discordant U-Pb zircon ages: An  
850 evaluation. *Journal of Metamorphic Geology*, 15(1), 127–140.  
851 <https://doi.org/10.1111/j.1525-1314.1997.00008.x>
- 852 Miller, J. S., Matzel, J. E. P., Miller, C. F., Burgess, S. D., & Miller, R. B. (2007). Zircon growth and  
853 recycling during the assembly of large, composite arc plutons. *Journal of Volcanology and*  
854 *Geothermal Research*, 167(1–4), 282–299.  
855 <https://doi.org/10.1016/j.jvolgeores.2007.04.019>
- 856 Moore, W. B., & Webb, A. A. G. (2013). Heat-pipe Earth. *Nature*, 501(7468), 501–505.  
857 <https://doi.org/10.1038/nature12473>
- 858 Morón, S., Kohn, B. P., Beucher, R., Mackintosh, V., Cawood, P. A., Moresi, L., & Gallagher, S. J.  
859 (2020). Denuding a Craton: Thermochronology Record of Phanerozoic Unroofing From the  
860 Pilbara Craton, Australia. *Tectonics*, 39(9). <https://doi.org/10.1029/2019TC005988>
- 861 Mundil, R., Ludwig, K. R., Metcalfe, I., & Renne, P. R. (2004). Age and Timing of the Permian  
862 Mass Extinctions: U/Pb Dating of Closed-System Zircons. *Science*, 305, 1760–1762.  
863 [www.sciencemag.org](http://www.sciencemag.org)
- 864 Naeser, C. W., Naeser, N. D., Newell, W. L., Southworth, S., Edwards, L. E., & Weems, R. E.  
865 (2016). Erosional and depositional history of the Atlantic passive margin as recorded in  
866 detrital zircon fission-track ages and lithic detritus in Atlantic Coastal plain sediments.  
867 *American Journal of Science*, 316(2), 110–168. <https://doi.org/10.2475/02.2016.02>



- 868 Nasdala, L., Reiners, P. W., Garver, J. I., Kennedy, A. K., Stern, R. A., Balan, E., & Wirth, R. (2004).  
869 Incomplete retention of radiation damage in zircon from Sri Lanka. *American Mineralogist*,  
870 *89*, 219–231.
- 871 Nasdala, L., Wenzel, M., Vavra, G., Irmer, G., Wenzel, T., & Kober, B. (2001). Metamictisation of  
872 natural zircon: Accumulation versus thermal annealing of radioactivity-induced damage.  
873 *Contributions to Mineralogy and Petrology*, *141*(2), 125–144.  
874 <https://doi.org/10.1007/s004100000235>
- 875 O'Connor, L., Szymanowski, D., Eddy, M. P., Samperton, K. M., & Schoene, B. (2022). A red bole  
876 zircon record of cryptic silicic volcanism in the Deccan Traps, India. *Geology*, *50*(4), 460–  
877 464. <https://doi.org/10.1130/G49613.1>
- 878 Paces, J. B., & Miller, J. D. (1993). Precise U-Pb ages of Duluth Complex and related mafic  
879 intrusions, northeastern Minnesota: geochronological insights to physical, petrogenetic,  
880 paleomagnetic, and tectonomagmatic processes associated with the 1.1 Ga Midcontinent  
881 Rift system. *Journal of Geophysical Research*, *98*(B8). <https://doi.org/10.1029/93jb01159>
- 882 Palenik, C. S., Nasdala, L., & Ewing, R. C. (2003). Radiation damage in zircon. *American*  
883 *Mineralogist*, *88*, 770–781.
- 884 Peterman, E. M., Reddy, S. M., Saxey, D. W., Fougereuse, D., Snoeyenbos, D. R., & Rickard, W.  
885 D. A. (2019). Nanoscale processes of trace element mobility in metamorphosed zircon.  
886 *Contributions to Mineralogy and Petrology*, *174*(11). <https://doi.org/10.1007/s00410-019-1631-1>
- 887
- 888 Peterman, E. M., Reddy, S. M., Saxey, D. W., Fougereuse, D., Zakaria Quadir, M., & Jercinovic,  
889 M. J. (2021). Trace-element segregation to dislocation loops in experimentally heated  
890 zircon. *American Mineralogist*, *106*(12), 1971–1979. <https://doi.org/10.2138/am-2021-7654>
- 891
- 892 Reddy, S. M., van Riessen, A., Saxey, D. W., Johnson, T. E., Rickard, W. D. A., Fougereuse, D.,  
893 Fischer, S., Prosa, T. J., Rice, K. P., Reinhard, D. A., Chen, Y., & Olson, D. (2016).  
894 Mechanisms of deformation-induced trace element migration in zircon resolved by atom  
895 probe and correlative microscopy. *Geochimica et Cosmochimica Acta*, *195*, 158–170.  
896 <https://doi.org/10.1016/j.gca.2016.09.019>
- 897 Reiners, P. W., Spell, T. L., Nicolescu, S., & Zanetti, K. A. (2004). Zircon (U-Th)/He  
898 thermochronometry: He diffusion and comparisons with <sup>40</sup>Ar/<sup>39</sup>Ar dating. *Geochimica et*  
899 *Cosmochimica Acta*, *68*(8), 1857–1887. <https://doi.org/10.1016/j.gca.2003.10.021>
- 900 Roden, M. K. (1991). Apatite Fission-Track Thermochronology of the Southern Appalachian  
901 Basin: Maryland, West Virginia, and Virginia. *The Journal of Geology*, *99*(1), 41–53.  
902 <https://doi.org/10.1086/629472>
- 903 Schmitz, M. D., Bowring, S. A., & Ireland, T. R. (2003). *Evaluation of Duluth Complex anorthositic*  
904 *series (AS3) zircon as a U-Pb geochronological standard: New high-precision isotope*  
905 *dilution thermal ionization mass spectrometry results*. [https://doi.org/10.1016/S0016-7037\(00\)00200-X](https://doi.org/10.1016/S0016-7037(00)00200-X)
- 906
- 907 Schoene, B. (2014). U–Th–Pb Geochronology. In *Treatise on Geochemistry* (pp. 341–378).  
908 Elsevier. <https://doi.org/10.1016/B978-0-08-095975-7.00310-7>
- 909 Schoene, B., Crowley, J. L., Condon, D. J., Schmitz, M. D., & Bowring, S. A. (2006). Reassessing  
910 the uranium decay constants for geochronology using ID-TIMS U-Pb data. *Geochimica et*  
911 *Cosmochimica Acta*, *70*(2), 426–445. <https://doi.org/10.1016/j.gca.2005.09.007>



- 912 Schoene, B., Latkoczy, C., Schaltegger, U., & Günther, D. (2010). A new method integrating high-  
913 precision U-Pb geochronology with zircon trace element analysis (U-Pb TIMS-TEA).  
914 *Geochimica et Cosmochimica Acta*, 74(24), 7144–7159.  
915 <https://doi.org/10.1016/j.gca.2010.09.016>
- 916 Smithies, R. H., Champion, D. C., & Cassidy, K. F. (2003). Formation of Earth's early Archaean  
917 continental crust. *Precambrian Research*, 127(1–3), 89–101.  
918 [https://doi.org/10.1016/S0301-9268\(03\)00182-7](https://doi.org/10.1016/S0301-9268(03)00182-7)
- 919 Swanson-Hysell, N. L., Hoaglund, S. A., Crowley, J. L., Schmitz, M. D., Zhang, Y., & Miller, J. D.  
920 (2020). Rapid emplacement of massive Duluth Complex intrusions within the North  
921 American Midcontinent Rift. *Geology*, 49(2), 185–189. <https://doi.org/10.1130/G47873.1>
- 922 Swanson-Hysell, N. L., Ramezani, J., Fairchild, L. M., & Rose, I. R. (2019). Failed rifting and fast  
923 drifting: Midcontinent Rift development, Laurentia's rapid motion and the driver of  
924 Grenvillian orogenesis. *Bulletin of the Geological Society of America*, 131(5–6), 913–940.  
925 <https://doi.org/10.1130/B31944.1>
- 926 Szymanowski, D., & Schoene, B. (2020). U–Pb ID-TIMS geochronology using ATONA amplifiers.  
927 *Journal of Analytical Atomic Spectrometry*, 35(6), 1207–1216.  
928 <https://doi.org/10.1039/D0JA00135J>
- 929 Takehara, M., Horie, K., Hokada, T., & Kiyokawa, S. (2018). New insight into disturbance of U-Pb  
930 and trace-element systems in hydrothermally altered zircon via SHRIMP analyses of zircon  
931 from the Duluth Gabbro. *Chemical Geology*, 484, 168–178.  
932 <https://doi.org/10.1016/j.chemgeo.2018.01.028>
- 933 Todt, W. A., & Büsch, W. (1981). U-Pb investigations on zircons from pre-Variscan gneisses-I. A  
934 study from the Schwarzwald, West Germany. *Geochimica et Cosmochimica Acta*, 45, 1789–  
935 1801.
- 936 Van Kranendonk, M. J., Hugh Smithies, R., Hickman, A. H., & Champion, D. C. (2007). Review:  
937 Secular tectonic evolution of Archean continental crust: interplay between horizontal and  
938 vertical processes in the formation of the Pilbara Craton, Australia. In *Terra Nova* (Vol. 19,  
939 Issue 1, pp. 1–38). <https://doi.org/10.1111/j.1365-3121.2006.00723.x>
- 940 Weber, W. J. (1990). Radiation-induced defects and amorphization in zircon. *J. Mater. Res.*,  
941 5(11), 2687–2697. <http://journals.cambridge.org>
- 942 Weber, W. J. (1993). Alpha-Decay-Induced Amorphization in Complex Silicate Structures.  
943 *Journal of the American Ceramic Society*, 76(7), 1729–1738.  
944 <https://doi.org/10.1111/j.1151-2916.1993.tb06641.x>
- 945 Widmann, P., Davies, J. H. F. L., & Schaltegger, U. (2019). Calibrating chemical abrasion: Its  
946 effects on zircon crystal structure, chemical composition and U–Pb age. *Chemical Geology*,  
947 511, 1–10. <https://doi.org/10.1016/j.chemgeo.2019.02.026>
- 948 Wiemer, D., Allen, C. M., Murphy, D. T., & Kinaev, I. (2017). Effects of thermal annealing and  
949 chemical abrasion on ca. 3.5 Ga metamict zircon and evidence for natural reverse  
950 discordance: Insights for U[ $\text{Pb}$ ] LA-ICP-MS dating. *Chemical Geology*, 466, 285–302.  
951 <https://doi.org/10.1016/j.chemgeo.2017.06.019>
- 952 Williams, I. S., Compston, W., Black, L. P., Ireland, T. R., & Foster, J. J. (1984). Contributions to  
953 Mineralogy and Petrology Unsupported radiogenic Pb in zircon: a cause of anomalously  
954 high Pb-Pb, U-Pb and Th-Pb ages. In *Contrib Mineral Petrol* (Vol. 88).



955 Yamada, R., Murakami, M., & Tagami, T. (2007). Statistical modelling of annealing kinetics  
956 of fission tracks in zircon; Reassessment of laboratory experiments. *Chemical*  
957 *Geology*, 236(1–2), 75–91. <https://doi.org/10.1016/j.chemgeo.2006.09.002>